Observations of Titan's Northern lakes at 5 μm: Implications for the organic cycle and geology

C. Sotin [a,*], K.J. Lawrence [a], B. Reinhardt [a], J.W. Barnes [b], R.H. Brown [c], A.G. Hayes [a], S. Le Mouélic [d], S. Rodriguez [e], J.M. Soderblom [c], L.A. Soderblom [f], K.H. Baines [a], B.J. Buratti [a], R.N. Clark [g], R. Jaumann [h], P.D. Nicholson [i], K. Stephan [h]

[a] Jet Propulsion Laboratory, Caltech, 4800 Oak Grove Drive, Pasadena, CA 91109, USA
[b] Department of Physics, University of Idaho, Engineering-Physics Building, Moscow, ID 83844, USA
[c] Department of Planetary Sciences, University of Arizona, Lunar and Planetary Laboratory, 1629 E. University Blvd., Tucson, AZ 85721, USA
[d] Laboratoire de Planétologie et Géodynamique, CNRS-UMR 6112, Université de Nantes, 2 rue de la Houssinière, 44322 Nantes, France
[e] Laboratoire AIM, Université Paris Diderot, Paris 7/CNRS/CEA-Saclay, DSM/IRFU/SAp, France
[f] United States Geological Survey, 2255 N. Gemini Drive, Flagstaff, AZ 86001, USA
[g] United States Geological Survey, Mail Stop 964, Box 25046, Denver Federal Center, Denver, CO 80225, USA
[h] DLR, Institute of Planetary Research, Rutherfordstrasse 2, D-12489 Berlin, Germany
[i] Department of Astronomy, Cornell University, 418 Space Sciences Building, Ithaca, NY 14853, USA

ARTICLE INFO

ABSTRACT

Since Titan entered Northern spring in August 2009, the North Pole has been illuminated allowing observations at optical wavelengths. On June 5, 2010 the Visual and Infrared Mapping Spectrometer (VIMS) onboard the Cassini spacecraft observed the Northern Pole area with a pixel size from 3 to 7 km. Since, as we demonstrate, little of the solar flux at 5 μm is scattered by the atmosphere, these observations were obtained at relatively large incidence angles and allowed us to build a mosaic covering an area of more than 500,000 km^2 that overlaps and complements observations made by the Synthetic Aperture Radar (SAR) in 2007. We find that there is an excellent correlation between the shape of the radar dark area, known as Ligeia Mare and the VIMS 5-μm dark unit. Matching most of the radar shoreline, the 2010 VIMS observations suggest that the 125,000-km^2 surface area of Ligeia Mare measured by RADAR in 2007 has not significantly changed. The VIMS observations complement the radar observations to the west of Ligeia Mare and suggest that Ligeia Mare is connected to Kraken Mare by either a diffuse network similar to a swamp area, or by well-defined, sub-pixel rivers. Considering the results of recent evaporation models of methane, our preferred interpretation of the relative constancy in surface area of Ligeia is that it is principally composed of ethane although we cannot rule out the possibility that methane evaporation is balanced with replenishment by either precipitation or underground seepage. There is also strong correlation between the location of the small radar lakes and the small VIMS 5-μm dark patches. The geographic location of the small lakes are within a VIMS pixel of the SAR location, suggesting that the non-synchronous component of Titan's spin rate, if it exists, was less than 2.3×10^{-4} deg/day between 2007 and 2010 in agreement with the recent T64 radar observations. These observations question the existence of non-synchronous rotation. Two radar-bright features appear dark at 5-μm. The simplest interpretation is that these are very shallow lakes, less than one meter deep. Three new small lakes, named Freeman, Cardiel, and Towada by the IAU, are found outside of the area mapped with the SAR. A single-scattering model describing reflection of sunlight at 5-μm suggests that the lake surface is mirror-like and that the albedo of the solid surfaces surrounding the lakes is about 8%. These observations together with information of the haze aerosols allow us to show that Titan's lakes, atmospheric ethane and aerosol haze are smaller carbon reservoirs than Titan's sand dunes and atmospheric methane. A simple model involving an outburst of methane a few hundreds of Myr ago followed by the dissociation of methane in the atmosphere leading to the formation of the haze particles that constitute the dune fields would be consistent with both the present observations and recent measurements of isotopic ratios in atmospheric methane (Mandt, K.E. et al. [2012]. Astrophys. J. 749(160), 14).

* Corresponding author. Address: Jet Propulsion Laboratory, M/S 183-301, 4800 Oak Grove Drive, Pasadena, CA 91109, USA.
E-mail address: Christophe.sotin@jpl.nasa.gov (C. Sotin).

1. Introduction

Titan, Saturn's largest moon, is the only object in the Solar System, besides Earth, to support stable bodies of liquids at its surface (Stofan et al., 2007; Brown et al., 2008; Hayes et al., 2008; Stephan et al., 2010). In the Northern polar area, the Imaging Science Sub System (ISS) first imaged Kraken Mare (Turtle et al., 2009), the largest liquid body on Titan, with shorelines at latitudes as low as 50°N. Then, the Synthetic Aperture Radar (SAR) instrument acquired high resolution swaths over these areas, discovering tens of smaller lakes as well as two other large bodies of liquid named Punga and Ligeia Mares (Stofan et al., 2007). Each of the three large lakes covers an area more than 100,000 km^2 (Hayes et al., 2008). The radar coverage is not yet complete, and one pending question is whether Kraken Mare and Ligeia Mare are connected.

Nearly 48% of Titan's surface has been observed by the radar instrument to date with more than 60% coverage in the Northern hemisphere. The observations suggest that the liquid bodies are more numerous in the Northern hemisphere than in the Southern hemisphere, which has been attributed to a cycle similar to Earth's Milankovich cycles (Aharonson et al., 2009). Since Saturn's equinox in August 2009, the Titan's North Pole has gradually become illuminated, and the opacity of its North polar hood has decreased (Le Mouelic et al., 2012). As a result, the Northern lakes have become visible at optical/infrared wavelengths. The Visual and Infrared Mapping Spectrometer (VIMS) observed these lakes when Cassini was close to Titan during the T69 flyby in June 2010. A global map of the lakes, complementing the RADAR observations, has been generated with a pixel size between 3 and 7-km between latitudes 65–75°N and longitudes 60–190°E (Section 2).

Understanding the carbon cycle on Titan requires a better knowledge of the processes governing the chemical evolution of the carbon-bearing molecules and their storage in different reservoirs. Methane is the most abundant carbon-bearing molecule in Titan's atmosphere. It is irreversibly transformed into ethane and other higher order hydrocarbons and nitriles by photolysis. The Huygens probe, which landed in the equatorial region, measured methane concentrations from 1.48% in the upper atmosphere up to 5.67% near the surface (Niemann et al., 2010). During the first 2 min after touchdown the methane concentration rose abruptly suggesting methane moisture in the subsurface was being exhausted by the warm GCMS inlet driven into the soil (Niemann et al., 2005). Different sources of methane have been invoked to explain its present presence and abundance on Titan, including storage in lakes (Mitri et al., 2007), subsurface reservoirs (Mousis and Schmitt, 2008) and/or deep reservoirs (Atreya et al., 2006). Thermodynamic calculations assuming equilibrium between the atmosphere and the lakes predict that the lakes are mostly composed of ethane (76–79%), propane (~7–8%) and methane (~5–10%) with small amounts of hydrogen cyanide, butene, and acetylene (Cordier et al., 2009). The VIMS observations of Ontario Lacus (Brown et al., 2008) demonstrated that liquid ethane is indeed present in the lakes. However lakes and atmosphere are most likely not in equilibrium since the events related to the replenishment of the lakes (rain, evaporation, seasonal oscillations) may have timescales shorter than do the kinetics involved in equilibrating the lakes with the atmosphere. Determining the evolution of the surface area covered by lakes provides constraints on the volume of these reservoirs and their lifetimes (Section 3).

The small lakes are distinct surface features that are not only intrinsically interesting but also can be used to constrain Titan's rotational and orbital dynamics, the detailed knowledge of which is not only important for constraining Titan's interior but also for mapping and targeting specific features. Provided the VIMS images can be navigated with sufficient accuracy, mapping small, discrete, well-isolated lakes provides a means to monitor Titan's spin rate and to check whether it is synchronous with its orbital rotation (Section 4).

2. Geological context and data acquisition, processing and analysis

The VIMS instrument simultaneously acquires intensity measurements in 352 wavelength bands from 0.35- to 5.12-μm. Titan's atmosphere scatters and absorbs most of the photons in the VIMS spectral range except in five narrow atmospheric bands centered at 0.933-, 1.082-, 1.270-, 1.590-, and 2.019-μm and two broader atmospheric bands between 2.615- and 2.947-μm and between 4.903- and 5.122-μm (Sotin et al., 2005). In these atmospheric windows, scattering by the atmospheric molecules and by the aerosols must be taken into account in order to retrieve the surface properties (Rodriguez et al., 2006). The influence of scattering decreases with increasing wavelength and is almost negligible at 5-μm (Rodriguez et al., 2006; Soderblom et al., 2007a,b). Each image is usually 64×64 pixels, though smaller images can be acquired depending on circumstances. For example, when the VIMS instrument rides along with instruments that scan Titan, we use a line mode, equivalent to a push-broom mode, with the width and integration time adjusted to the scan velocity. The T69 flyby is one of three flybys that were allocated to VIMS at closest approach (C/A) during the Cassini Equinox Mission, and was the first flyby above the lake district of the Northern high latitudes. The image cubes (Table 1) were acquired on June 5th 2010 during the segment named VIMS_132TI_REGMAP001 which started at 2:11:27 UTC, about 15 min before C/A and ended at 4:26:27 UTC. The C/A distance was about 2050 km, which provides an optimal footprint of about 1 km/pixel with nadir pointing (Table 1) when the spacecraft was near the North Pole (87.3°N; 9.4°W).

Cassini began the T69 flyby at 35°N and moved towards Titan's North Pole along the sub-Saturn meridian. After closest-approach, it receded from Titan near 207°W longitude and latitudes near 30°N (Fig. 1) with a phase angle (Sun–Titan's center – S/C) near 30°. Although the phase angle was larger than 90° prior to C/A, the polar area was illuminated. The incidence angle of the high-resolution observations close to the North Pole was very large (up to 90°). We can note that the surface just beyond the terminator was visible, illuminated by scattering haze. The first cube acquired during the flyby was obtained before C/A, and was designed to observe specular reflection similar to that seen during the T57 flyby (Stephan et al., 2010). No such reflection was observed in cube I (Fig. 1), demonstrating the lack of a liquid surface in the area it covered (78–80°N, 60–90°W). This observation is consistent with radar observations of this area (see map by Hayes et al. (2008)). Furthermore, no surface morphology could be observed using this image cube because of the poor illumination conditions. While the tangential velocity of the S/C relative to Titan was very high (6 km/s at C/A during this flyby) VIMS acquired data using its line-mode where a transect across the surface was obtained by repeatedly taking short exposures in a single VIMS line of pixels in order to maximize surface coverage. The second 64×64 cube was obtained as the spacecraft flew over mid-latitudes and all of the subsequent cubes were taken with large emission angles with the last cube as high as 80°.

The size of the pixel footprint depends on three geometric parameters: (i) the distance of the spacecraft to Titan's surface (sub-spacecraft altitude), (ii) the distance of the targeted area from the sub-spacecraft point, and (iii) the emission angle. Although the S/C was moving very quickly away from the Pole towards the equatorial latitudes (Fig. 2), the goal of this observation sequence was to obtain a mosaic of the illuminated region near the North Pole. The strategy was to acquire a high resolution cube (cube III in Table 1

Table 1
(A) Characteristics of the nine VIMS cubes acquired during the closest approach (C/A) segment of flyby T69 on June 5th, 2010 (VIMS_132TI_REGMAP001). Closest approach time was 2:26:26 when the spacecraft was at 2044 km from Titan's surface. Only the first cube was acquired before C/A with a phase angle larger than 90°. The first table gives the three cubes acquired with an integration time of 60 ms. The table (B) gives the list of cubes acquired with longer integration times. These cubes are given roman numbers (I–IX) and are located in Fig. 1. The value of the parameter 'scale' is the width of the field of view at Titan's surface. The pixel surface area is the square of the scale divided by the cosine of the emission angle which varies for each pixel.

A		Latitude	Longitude	Phase	Incidence	Emission
I – 1,654,398,195 T02:18:04 – T02:22:24 (60 ms) – scale = 2.2/1.6 km						
Center	(32,32)	80.2501	280.795	133.1	78.7	56.5
Top Lft	(1,1)	78.0783	278.769	139.2	76.9	65.2
Btm Lft	(1,63)	79.7366	270.689	126.2	77.2	50
Btm Rt	(63,63)	81.7116	282.339	124.1	79.9	45.3
Top Rt	(63,1)	80.6971	301.96	137.3	81.8	58.6
II – 1,654,399,210 T02:35:00 – T02:39:20 (60 ms) – scale = 2.1/2.8 km						
Center	(32,32)	79.8684	244.625	43.6	75.5	48.8
Top Lft	(1,1)	78.9796	252.194	49.6	75	43.1
Btm Lft	(1,63)	77.0149	236.917	41.2	72.6	49.4
Btm Rt	(63,63)	80.1119	231.014	39.4	75.7	52.1
Top Rt	(63,1)	81.4506	253.899	47.6	77.4	45.5
III – 1,654,399,736 T02:43:45 – T02:48:05 (60 ms) – scale = 3.3/3.9 km						
Center	(32,32)	75.694	227.884	35	71.4	56.8
Top Lft	(1,1)	76.2199	241.695	37.1	71.8	57.3
Btm Lft	(1,63)	70.4428	226.02	35	66.3	52.8
Btm Rt	(63,63)	73.6204	213.831	33.2	70.5	55.2
Top Rt	(63,1)	80.2727	233.867	35.3	75.8	60.1
B						
IV – 1,654,400,219 T02:51:48 – T03:03:21 (160 ms) – scale = 4.6/6.2 km						
Center	(32,32)	73.9597	266.65	34	71.8	71.4
Top Lft	(1,1)	70.2124	313.721	36.2	81.5	84
Btm Lft	(1,63)	65.5606	251.681	34.1	62	63.8
Btm Rt	(63,63)	69.1202	231.917	32.3	64.8	60.9
Top Rt	(63,1)	76.5504	318.334	34.3	83.8	82.4
V – 1,654,401,134 T03:07:03 – T03:18:36 (160 ms) – scale = 6.5/8.1 km						
Center	(32,32)	73.9513	224.936	31	69.9	67
Upr Lft	(1,7)	77.4279	320.36	32.2	84.3	87.4
Btm Lft	(1,63)	60.9485	226.169	31.6	57.1	55.2
Btm Rt	(63,63)	62.0068	202.555	29.8	62.9	54.2
Upr Rt	(63,6)	85.5042	5.651	30.4	88.4	86.2
VI – 1,654,402,028 T03:21:57 – T03:39:16 (240 ms) – scale = 8.2/10.6 km						
Center	(32,32)	65.0988	183.238	28.9	71.5	61.8
Top Lft	(1,1)	87.92	192.722	30	84.1	82.1
Btm Lft	(1,63)	50.6693	200.223	29.6	55.6	45
Btm Rt	(63,63)	49.2397	174.504	27.8	69.1	52.2
Upr Rt	(63,15)	73.1319	141.212	28.1	87.4	78.1
VII – 1,654,403,103 T03:39:52 – T03:48:32 (120 ms) – scale = 10.6/11.9 km						
Center	(32,32)	60.652	176.069	28.6	72.4	61
Top Lft	(1,1)	84.1983	94.765	29.5	90.2	88.1
Btm Lft	(1,63)	47.1294	197.779	29.5	54.6	42.6
Btm Rt	(63,63)	45.1262	170.211	27.7	70.8	52.3
Top Rt	(63,1)	65.6874	128.736	27.8	93.4	82
VIII – 1,654,403,828 T03:51:57 – T04:03:30 (160 ms) – scale = 12.5/14.2 km						
Center	(32,32)	65.0474	200.316	29.9	66.1	61.5
Top Lft	(1,1)	82.3417	280.099	30.8	80	84.5
Btm Lft	(1,63)	47.9061	218.405	30.7	46.5	44.7
Btm Rt	(63,63)	45.8267	187.355	29	60	45.3
Top Rt	(63,1)	76.6921	130.163	29	89.6	83.9
N Pole	(25,12)	88.6931	186.525	30.1	84.7	85.4
IX – 1,654,404,762 T04:07:31 – T04:14:17 (120 ms) – scale = 15.0/16.0 km						
Center	(32,32)	61.9368	238.221	31.2	57.5	63.4
Top Lft	(1,1)	62.8749	296.15	32.1	72.1	87.5
Btm Lft	(1,63)	51.5338	254.874	32.1	49.2	63.1
Btm Rt	(63,63)	49.8572	211.137	30.3	50.7	46.3
Top Rt	(63,1)	85.1196	229.481	30.4	80.7	82.8

and Fig. 2) with a relatively short integration time of 60 ms, and then acquire three cubes (cubes IV, V and VI in Table 1) with integration times of 160 ms (cubes IV and V) and 240 ms (cube VI). The longer integration time partly compensated for the increased attenuation of the surface emission affected by the increase in incidence angle. The pointing was designed to produce a mosaic of the area (Fig. 1). The flyby geometry produces footprints elongated in the meridian direction. The scale, which represents the width of a pixel projected onto the surface normal to the VIMS boresight, ranges from 3.3 km/pixel at the beginning of cube III acquisition to 10.6 km/pixel at the end of cube VI acquisition (Table 1). The footprint, which is the surface area of a pixel on Titan's surface, is the square of the width divided by the cosine of the emission angle (Table 1).

The raw VIMS data are then converted to units of I/F where I is the observed spectral radiance (W/m^2/sr/μm) on each of the 256

Table 2
Mean values and standard deviation of I/F in each window of each cube represented in the mosaic (Fig. 6). The albedo in the last column assumes that 45% of the light goes through the atmosphere as suggested by the scattering model detailed in Section 4.3.

Window Cube #	D1–7 detectors 2.03 (.05)		D2–12 detectors 2.72 (.09)		D3–14 detectors 5.0 (0.1)		Albedo @ D3
IV – 0219	0.0824	0.0033	0.0343	0.0045	0.0202	0.0039	7.4
V – 1134	0.0810	0.0031	0.0316	0.0047	0.0227	0.0051	6.8
VI – 2028	0.0761	0.0042	0.0284	0.0035	0.0242	0.0057	8.5
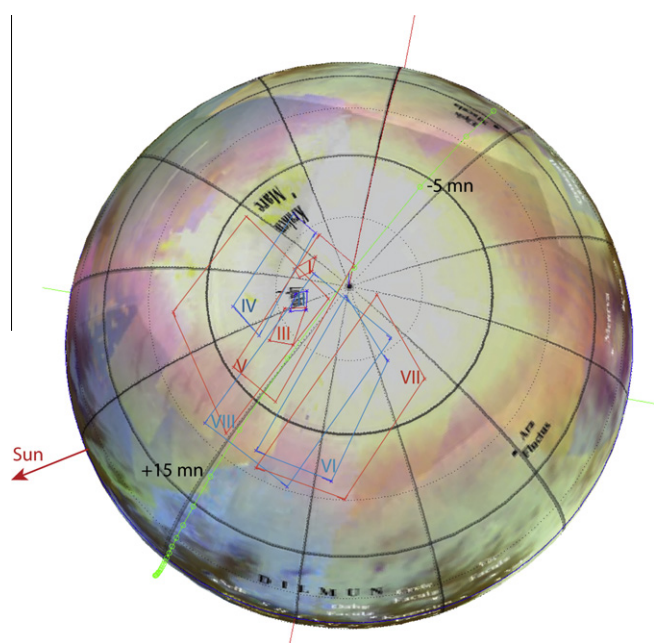
Fig. 1. Geometry of the flyby during the T69 VIMS observation. The locations of the different images are represented on the map with odd images in red and even images in blue. The subsolar point is indicated by the red arrow. The location of the sub spacecraft point is described by the green curve along which circles are 5 min apart. Closest approach occurred when the spacecraft was close to the North Pole. (For interpretation of the references to color in this figure legend, the reader is referred to the web version of this article.)

infrared (IR) detectors and πF is the incoming solar irradiance (W/m²/μm) at the location of the spacecraft (Brown et al., 2004). The intensity measured by VIMS includes a very strong contribution of light reflected by the haze (Rodriguez et al., 2006; Tomasko et al., 2008). The VIMS calibration pipeline includes removal of the background, a despiking algorithm to remove the effect of cosmic ray hits, a division by the flat-field acquired during calibration of the VIMS before launch and in flight, a conversion to specific intensity unit using VIMS spectro-radiometric response function (Brown et al., 2004) and the integration time, and a division by the solar spectrum (Thekaekara, 1973) at Titan's distance to the Sun (e.g. Barnes et al., 2007). VIMS' infrared channel has a mirror that scans in a (x, z) plane perpendicular to the boresight which is aligned with the $-Y$ axis of the spacecraft. It acquires images in 256 separate wavelengths of Titan's surface. The instantaneous field of view (IFOV) is 0.5 mrad. VIMS also has a high resolution mode which has a rectangular IFOV of 0.25×0.50 mrad (with the short dimension in the x-direction). The nominal mode is a scan of 64 pixels in each direction. A consequence of the observing geometry is distortion of the otherwise square image that makes the projection onto Titan's surface important. The projection of each pixel on Titan's surface is determined by using the navigation information including the geometry of the Cassini spacecraft, the orientation of the VIMS field of view relative to the spacecraft, and the Titan ephemerides. With detailed specification of the instrument data-acquisition timing, it is possible to determine the location of each pixel on Titan's surface. For the reconstruction of the images acquired during this flyby, we have used the kernel cpck02Feb2009.tpc which takes into account Titan's obliquity but assumes no precession (see discussion in Section 4.2). As noted below, the excellent correlation between the location of the lakes in the SAR images and in the VIMS cubes validates the process. The final step is to create an orthographic projection of the data centered at the North Pole (Fig. 3).

The VIMS instrument can observe Titan's surface in the seven infrared windows described above. The signal to noise (S/N) ratio of the data can be improved either by summing pixels of spectrally
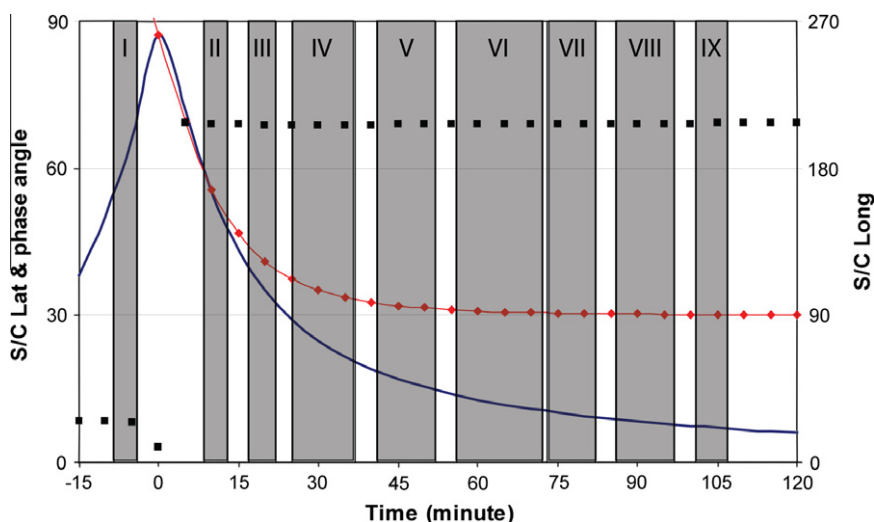

Fig. 2. Latitude, longitude, and phase angle versus time that is calculated relative to closest approach. The first image was taken facing the Sun (see Fig. 1 for the geometry) whereas the other images were taken with phase angles lower than 90°.
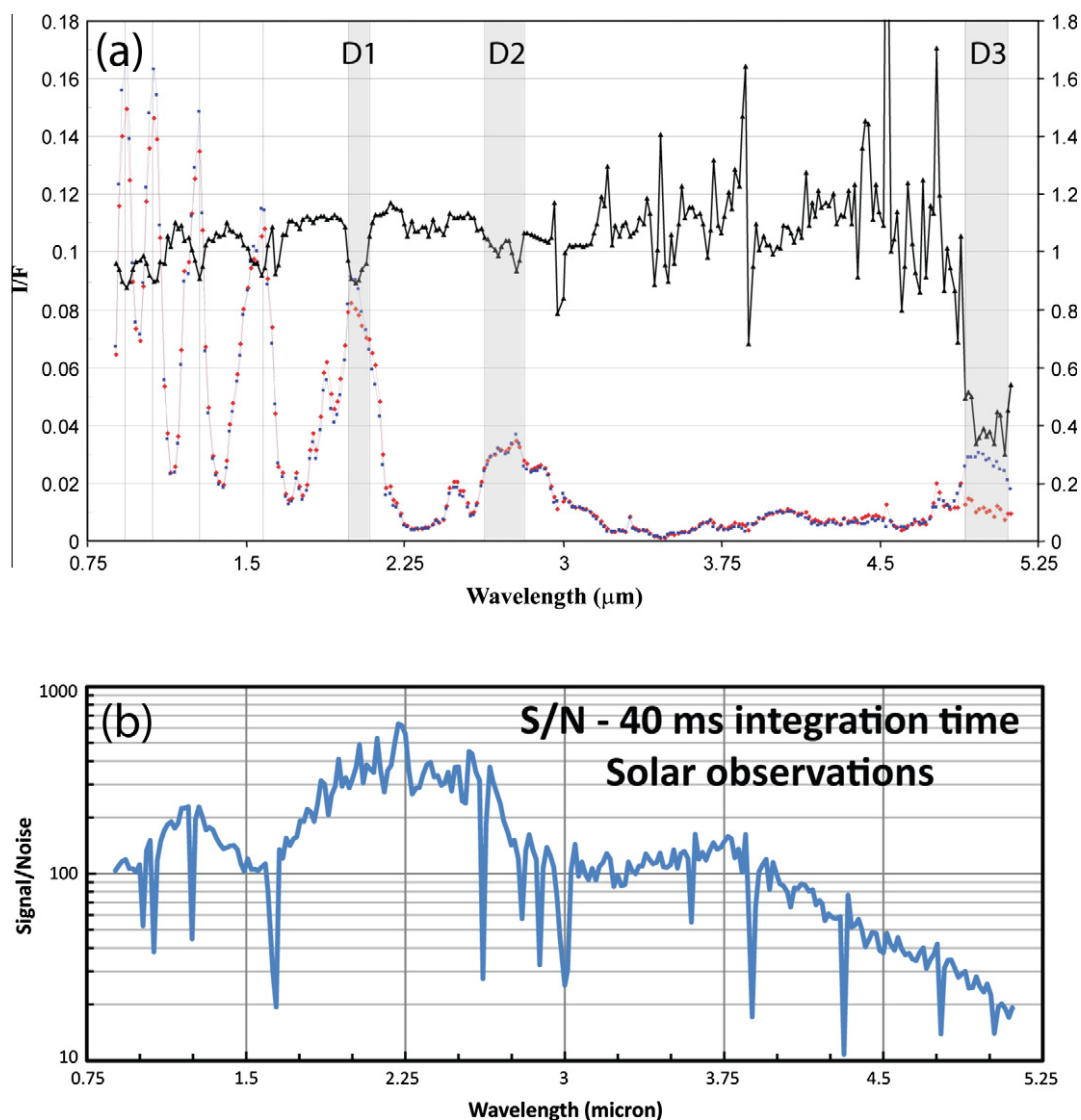
Fig. 3. (a) Spectra of the lake Ligeia (red line) and solid surface area (blue line) in cube IV. The ratio of the two is indicated by the dark line. The seven windows are indicated by the vertical lines and the three windows used in the present study are delineated in gray with D1, D2 and D3 centered at 2 μm, 2.7 μm, and 5 μm, respectively. (For interpretation of the references to color in this figure legend, the reader is referred to the web version of this article.) (b) Signal to Noise ratio inferred from solar occultation observations.

homogeneous areas observed with the same geometry or by spectral summing. The former is used to infer the composition; the latter is preferred to maintain the highest spatial resolution which is required for the morphological analysis performed in the present study. We define three spectral windows (Fig. 3 and Table 2): D1 from 1985 to 2084 nm (7 detectors), D2 from 2630 to 2816 nm (12 detectors) and D3 from 4903 to 5108 nm (14 detectors). The choice of D1 is driven by the very high S/N ratio (Fig. 3) combined with a good compromise between the solar flux and the scattering properties of the atmosphere (Sotin et al., 2005; Rodriguez et al., 2006). D2 and D3 are at higher wavelengths, which limits scattering in the atmosphere, and are broader windows, which allows us to add more channels and to improve the S/N ratio. Although there is very little light from the Sun at 5-μm, the spectral window D3 provides images with most contrast because scattering in Titan's atmosphere strongly decreases with wavelength (Section 3.1).

Cubes IV, V and VI were mosaicked for each spectral window (Fig. 4) and compared with the radar images obtained during flybys T28, T29, and T64 and using an orthographic projection centered at the North Pole. The radar instrument records the backscattered signal emitted from the spacecraft at a wavelength of 2.17 cm that

travels through Titan's atmosphere with little absorption (Rodriguez et al., 2003; Elachi et al., 2004). As can be seen, there is a very good correlation between the radar dark areas identified as lakes and Mares (Stofan et al., 2007) and the VIMS 5-μm dark areas; that is, the observed shoreline of Ligeia Mare is well matched and the radar-dark, small lakes appear at the same locations as the VIMS 5-μm dark areas. Unfortunately, the spectral windows D1 and D2 do not provide a clear view of the surface, so they are not considered further here. The next section describes the maps in detail and describes new lakes not observed by the radar. It also provides constraints on the albedo of Titan's solid surface at 5 μm, and it gives an upper limit for the non-synchronous component of Titan's spin rate. The analysis also suggests that the western part of Ligeia Mare is connected to Kraken Mare.

3. Results

The images obtained during the T69 flyby of Titan allow us to study three types of features: a large lake, Ligeia Mare (Section 3.2), small lakes (Section 3.3), and the solid surface near the North Pole
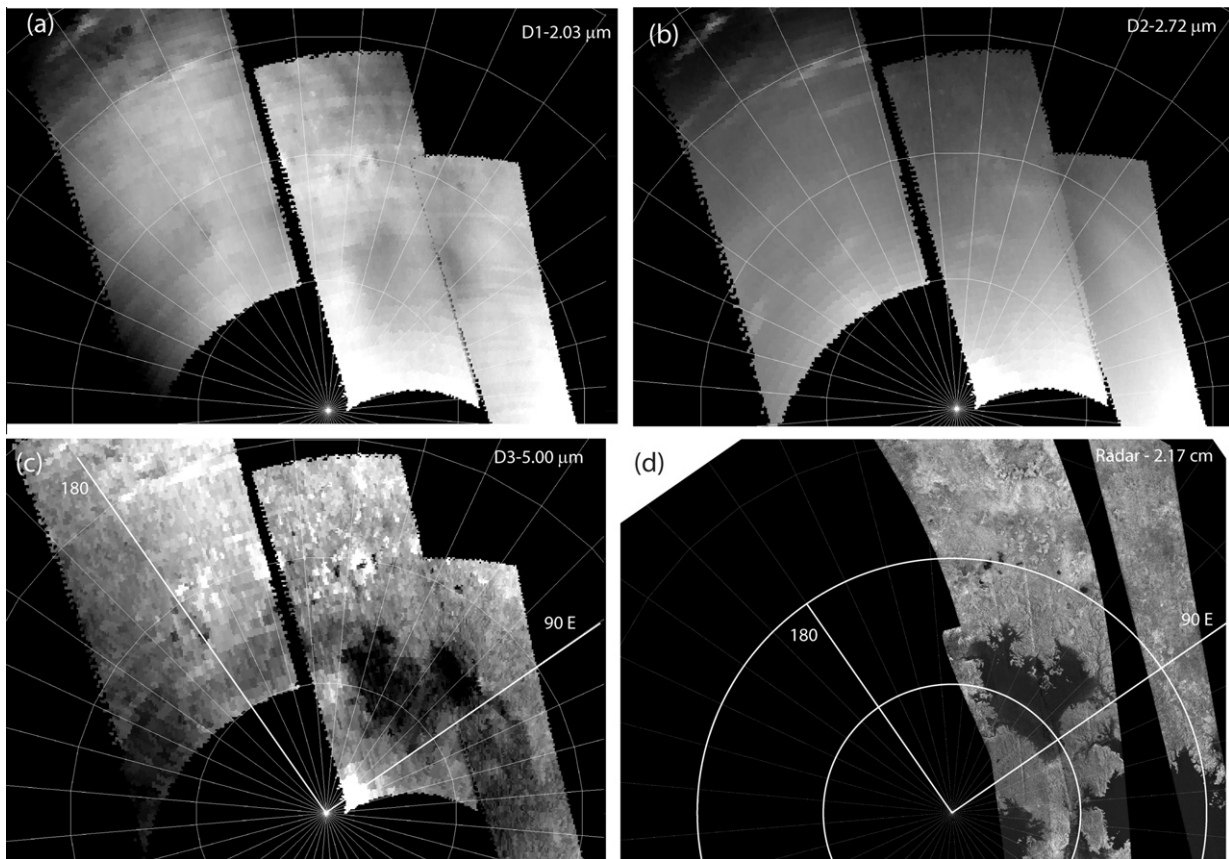
Fig. 4. Mosaics of the three spectral windows D1 (upper left), D2 (upper right), and D3 (lower left). These three mosaics can be compared with the radar map obtained by combining observations at T28 and T29 (lower right). Orthographic projections imply that the distance r on the map is proportional to sin(θ) where θ is the colatitude defined as $\theta = d/R$ where d is the real distance from the Pole along the meridian, and R is the Titan's radius. There is a clear correlation between surface features seen by radar and the D3 mosaic (see text for more details). Bright meridian features at 60°N on the VIMS mosaic of the spectral window D2 are clouds.

(Section 3.3). Implications of these observations for Titan's global evolution are discussed in Section 4.

3.1. Ligeia Mare

3.1.1. Brightness over Ligeia Mare

If the interaction between light and Titan's atmosphere were limited to absorption, the light collected by the VIMS instrument would come mostly from specular reflections over the lake's surface. Specular reflection geometry requires the emission and incidence angles to be coplanar to the surface normal and equal; the phase angle equals the sum of the two. Unfortunately the T69 flyby did not allow for such geometry over Ligeia Mare. In addition, the areas traced by the specular reflection groundtrack were mostly located south of latitude 50°N and did not intercept any bodies of liquid. When the specular reflection geometry occurs over a liquid body, it is indeed observed at 5-μm (Stephan et al., 2010; Barnes et al., 2011a,b; Soderblom et al., 2012) but not at shorter wavelengths due to the markedly increased atmospheric scattering.

Photons are absorbed and scattered by the molecules and aerosols in Titan's atmosphere. Analysis of the spectrum of the presumably dark lakes can provide useful information on the optical properties of the overlying atmosphere as backscattering by the surface is virtually non-existent there. In general, light reflected from Titan and collected by the VIMS camera consists of several components (e.g. Sobolev, 1975; Combes et al., 1991; Rodriguez et al., 2006) including: (1) direct light reflected by the surface, (2) light scattered in the atmosphere without interaction with the surface, (3) light reflected by the surface and then scattered

by the atmosphere into the beam of the instrument, (4) light scattered in the atmosphere and then reflected by the surface, (5) light reflected by the surface, scattered in the atmosphere back to the surface and then reflected to the instrument, and (6) all higher orders of surface-atmosphere multiple scattering that become diminishingly important with increasing order. Note that, in the presence of a dark surface, component (2) dominates and the light reflected from Titan's surface (1) will be less than observed elsewhere. Here, we assume the single-scattering, which is valid at 5-μm as discussed in Section 4.3. The plane-parallel atmosphere approximation is inadequate for this flyby when the incidence and emission angles were larger than 60°. The observed spectral radiance or intensity $I(\lambda, \phi)$ (in W/m²/μm/sr) is:

$$I(\lambda, \phi) = F(\lambda) \cdot \cos(i) \cdot R_S(\lambda) \cdot \exp(-\tau_{atm}) + I_{scattered}(\lambda, \phi) \qquad (1)$$

where λ is the wavelength, ϕ is the phase angle, F is the solar radiance (in W/m²/μm/sr), i is the incidence angle, R_S is the radiance factor ($R_S = \Pi$ with r being the bidirectional reflectance of a Lambert surface), τ_{atm} is the optical depth of the atmosphere, and $I_{scattered}$ a term that includes the components 2–6 described above.

The comparison between the VIMS mosaics and the radar map clearly shows that Ligeia Mare is darker than the surrounding solid surface at 2- and 5-μm (Fig. 4). It strongly suggests that the darkening is due to the lack of backscattering from the lake. For a path length in a clear hydrocarbon lake with a depth of 1- to 3-cm, all light in the 2- and 5-μm spectral windows would be absorbed except that which is specularly reflected which is 1–2% (Clark et al., 2010). The I/F amplitude at different wavelengths is plotted along a line that crosses the Ligeia Mare (Fig. 5). The most pronounced
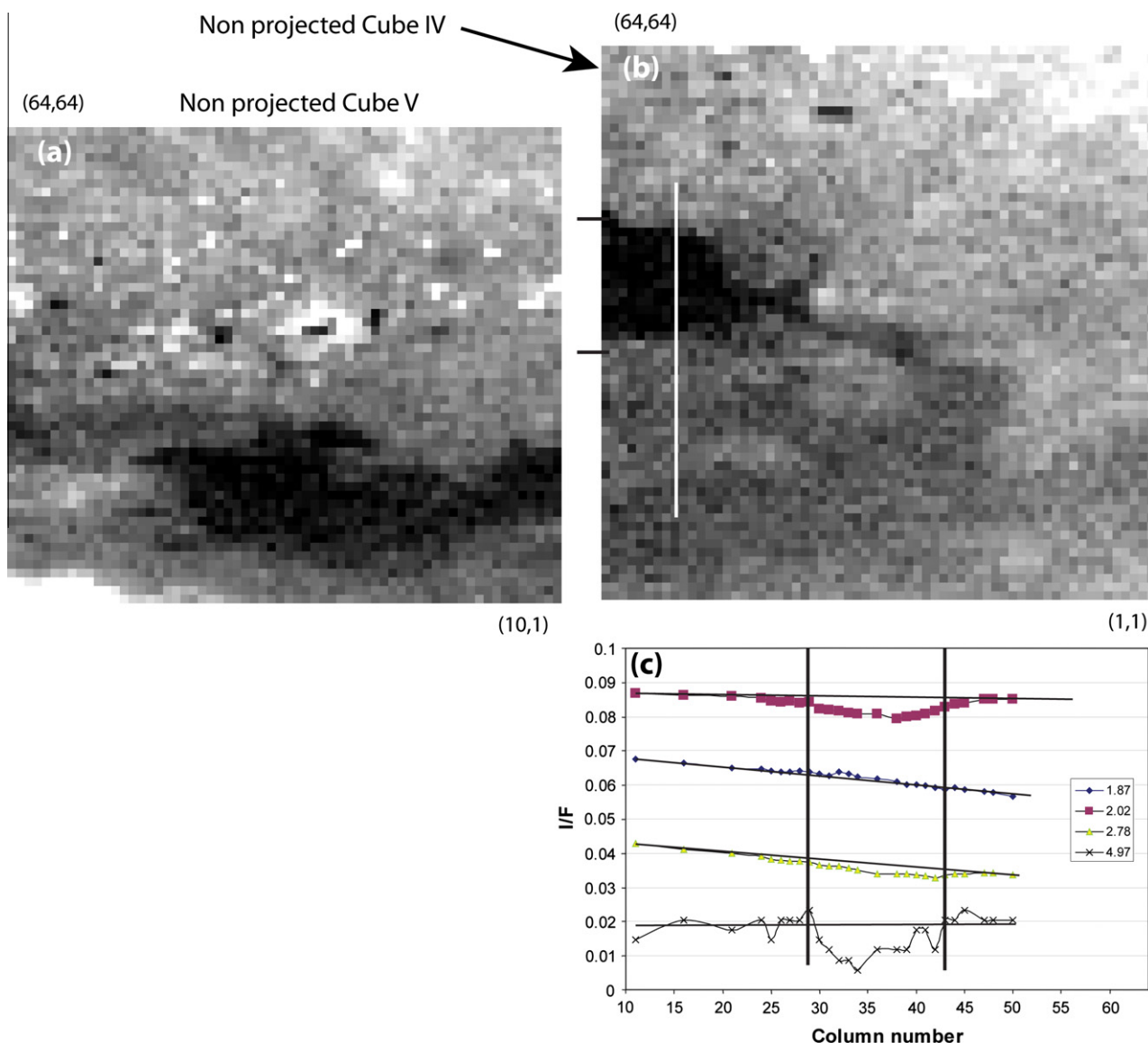
Fig. 5. The 5-μm images of the lake area clearly show the large Ligeia Mare as a wide dark area and the small lakes as dark pixels. Variations of I/F across Ligeia Mare (white vertical line in the upper right image) are shown at four wavelengths in the lower right panel. It emphasizes the strong potential of the 5-μm window to map Titan's surface. These two non-projected maps can be compared with Fig. 4 to emphasize the importance of the projection step.

contrast variations are at 5-μm because atmospheric scattering is nearly absent. Figs. 3 and 5 show that the 5-μm intensity is a factor of 2.5 less over Ligeia Mare relative to its surroundings. They also show that the amplitudes of these variations are much smaller at 2- and 2.8-μm than at 5 μm. The fraction of light reflected from the surface out to space is therefore larger at long wavelengths than at short wavelengths. This is due to the marked decrease in aerosol opacity with wavelength, as determined by Tomasko et al. (2008) and Bellucci et al. (2009) who find that the optical depth varies as λ^{-2}. For the dark lake surface, the main component is therefore the atmospheric component (2) with the addition of component (3) (light reflected on the solid surface and scattered in the beam of the VIMS instrument) for pixels near the shoreline, while at 5 μm, the main component is (3).

The I/F values of Ligeia Mare pixels in the D3 spectral window are around 1.35% (±0.2%) as shown in Fig. 6a. The values are geographically homogeneous (pixels with similar values of I/F are adjacent) including two very dark areas in the center of the Mare. These two dark patches are connected by a slightly brighter area,

but which is darker still than the surrounding terrains. A comparison between spectra acquired at the centers of the large lakes, at regions along the shore-lines and at regions of the surrounding terrains helps to constrain the atmospheric aerosol properties and to estimate the surface albedo at 5-μm (see Section 3.3). Over the two darkest spots of Ligeia Mare, the value of I/F at 5-μm seems to be independent of the incidence angle (Fig. 6a), which is consistent with only light scattered in the atmosphere being collected by the VIMS instrument. On the other hand, the I/Fs of the surrounding terrain show a linear trend (Fig. 6b) with an intercept at $\cos(i) = 0$ equal to 1.4%, which is within the uncertainties of the value of the dark areas of Ligeia Mare. This value is consistent with a lake reflectance equal to zero at 5-μm, an important result that shows that not only the surface is exceptionally dark, consistent with a >1 cm layer of liquid hydrocarbons, but as well rules out the presence of small particles of moderate or bright single-scattering albedo floating on the surface of the lake. However this observation does not rule out the presence of particles floating on or suspended in the lake that are substantially smaller than 5 μm.
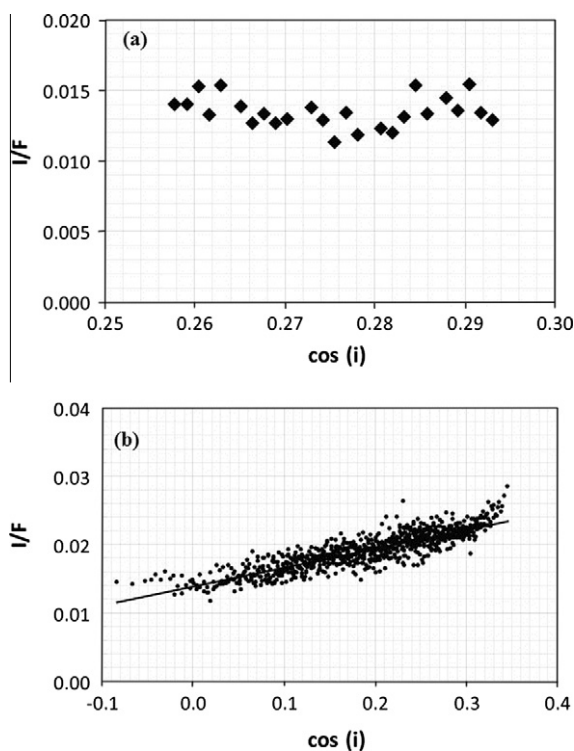
Fig. 6. The upper panel shows the values of I/F over Ligeia Mare versus the cosine of the incidence angle. There is no clear trend. On the other hand, I/F shows a linear trend versus cosine of the incidence angle for cube VI (Table 1). The slope is equal to 3.8%. As discussed in the text, this value implies a reflectance equal to 8% (±2%) at 5-μm.

3.1.2. Connection and comparison between Ligeia Mare and Kraken Mare

The North-polar region of Titan is home to three large lakes so-called Mare or seas named Punga, Kraken and Ligeia (Fig. 7). During T69, VIMS imaged the previously unobserved eastern tip of Kraken Mare (Fig. 7) yielding two intriguing results: first, the southwestern tip of Ligeia Mare seems to extend to Kraken Mare suggesting that two liquid bodies are connected, at least at the time of the VIMS observations; and second, the value of I/F at 5-μm over Kraken Mare is larger than that over Ligeia Mare.

On the radar map (Fig. 7), the southwestern tip of Ligeia is a place where the lake and associated rivers have complex interactions. In relatively flat topography, rivers are expected to meander and empty into the sea. This is clearly not the case for the rivers

around Ligeia Mare (Fig. 8). Near Ligeia, there are relatively short and wide depressions that are filled with liquids evidently flowing from the lakes, such as features labeled 1 (Fig. 8d). In contrast, nearby rivers (arrows 2 and 3 in Fig. 8d) are typically a few hundreds of kilometers in length, quite straight, do not meander toward Ligeia, and are usually well defined in radar maps. For example, the river indicated by arrow 2 travels northwest, getting very close to Ligeia but continues in the northwesterly direction crossing at nearly a right angle to other rivers (for example, river 4). The river 3 is parallel to river 2 and displays similar morphology before eventually ending in Ligeia Mare. In this area, the rivers form an interconnected network that seems independent of the mare. The linear pattern suggests tectonic control similar to that proposed for rivers carving the plateaus north of the Huygens Landing Site (Soderblom et al., 2007b) and for two thirds of the valley networks on Titan (Drummond et al., 2011). These are depressions possibly caused by tectonic activity. They would likely be filled with liquid hydrocarbons possibly from either rainfalls or seepage from a subsurface alkanifer. Choukroun and Sotin (2012) have proposed that the polar areas have undergone subsidence associated with the formation of ethane clathrates in the subsurface in order to explain Titan's shape. Such a model is consistent with the valley networks being controlled by tectonic activity. Alternatively, Soderblom et al. (2007a,b) suggested that some of the observed tectonic patterns may be pre-existing faults reactivated from cryovolcanism and filled with deposited material.

Another characteristic of these rivers is that they appear to overflow with a thin liquid layer extending on each side of the river (areas labeled 2 and 5 in Fig. 8d). This putative shallow zone, appearing wider and gray in the radar data, may come from Ligeia Mare and seems to be superimposed onto the narrow, radar dark, river in the center of the image. Alternatively, a similar radar backscattering echo would be obtained over a swampy area. The rivers are not resolved in the VIMS images but they do show a 5-μm-dark elongated, possibly wet area between the two mares (Figs. 4 and 7). This area (numbered 5 in Fig. 8d) extends to the west where there is no radar coverage, near longitude 90°E. The VIMS observations (Fig. 4) in this area suggest that the radar-dark area continues to the west and merges into Kraken Mare (area labeled K1 in Fig. 7).

VIMS observations further suggest that the three liquid bodies labeled K1, K2, and K3 (Fig. 7) are connected to each other. The area labeled 6 in Fig. 8 seems to be free of liquid to the south (right arrow) but is instead covered by a dense network of narrow rivers to the North (left arrow) that seem to connect area K3 with Ligeia Mare. The data show that area as dark at 5-μm, suggesting that is it either covered by a thin liquid layer or is a dense network of
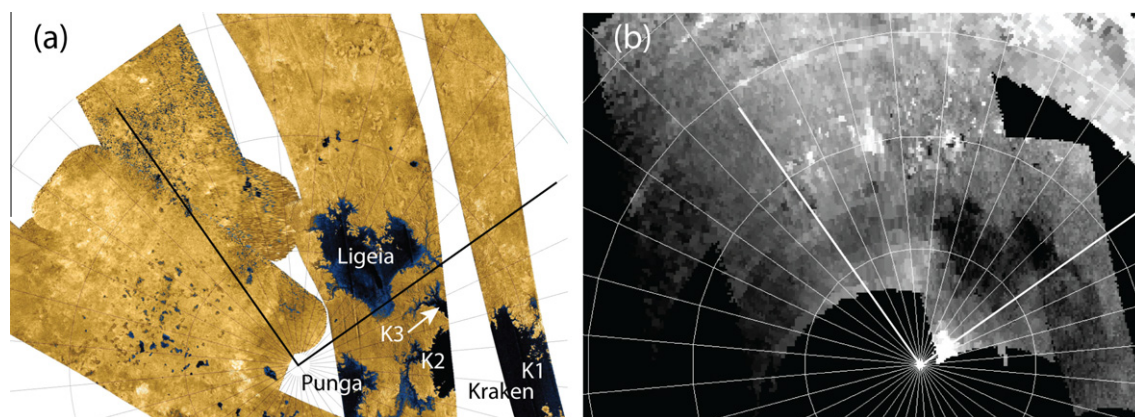

Fig. 7. Comparison between the VIMS 5-μm mosaic (right) obtained during T69 and the radar mosaic of this area (left). The longitudes 90°E and 180° are bold to ease the interpretation. Ligeia Mare can be seen in the center of the image. Portions of Kraken Mare and Punga Mare can be seen near the right edge and North Pole, respectively. The labels K1, K2, and K3 refer to different parts of Kraken Mare that appear interconnected in the VIMS mosaic.
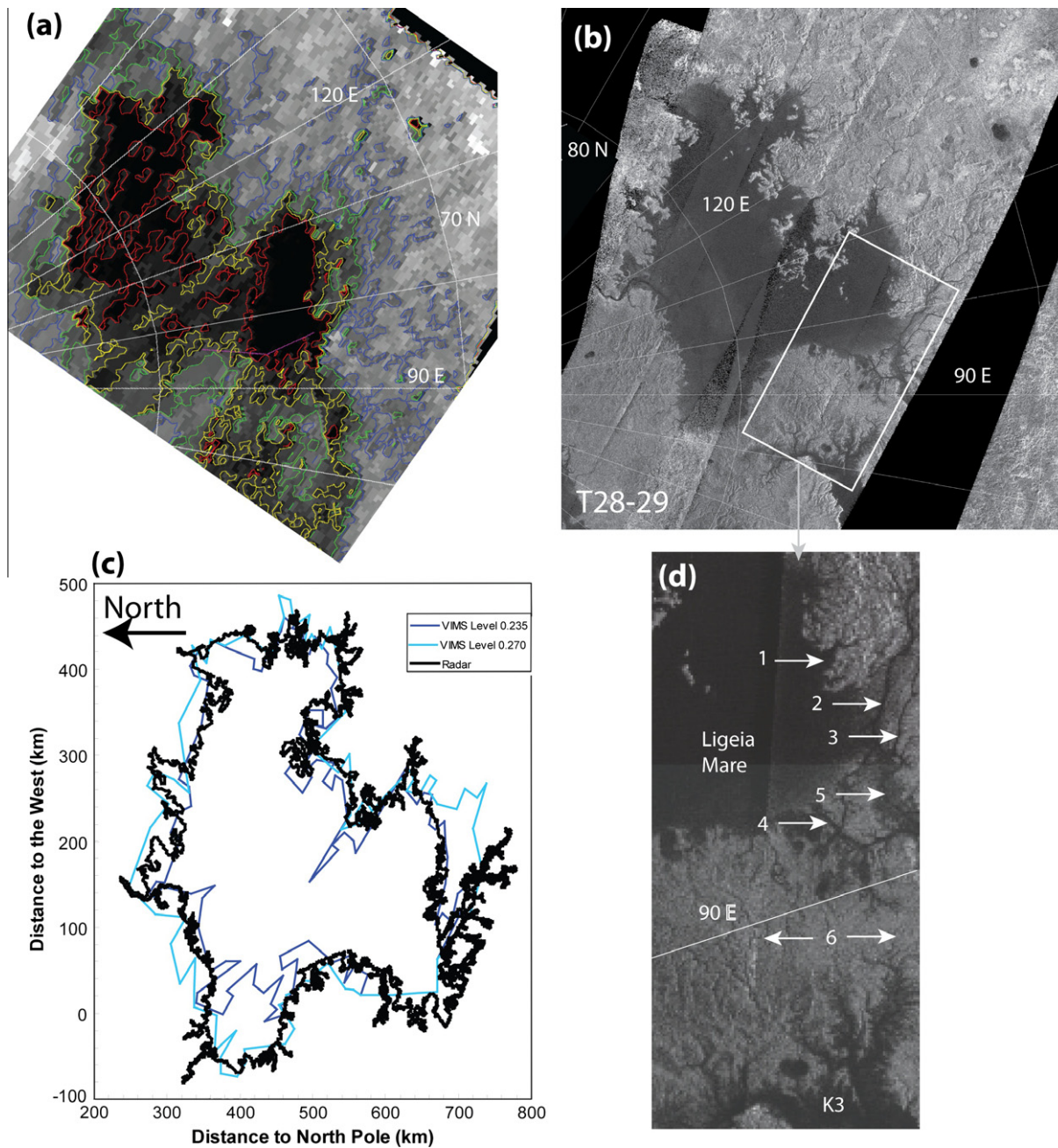
Fig. 8. Contour lines for spectral window D3 around Ligeia Mare. The contour levels are 0.200, 0.235, 0.270, and 0.300 for red, yellow, green, and blue, respectively. The upper right map shows the radar map of Ligeia Mare. The polar projections of the control points for radar (black) and contour lines 0.270 (dark blue) and 0.230 (light blue) are shown in the lower left panel. The lower right map is an enlargement of the western tip of Ligeia Mare showing different features (drown valleys, overflown rivers, rectangular network, dense river network) that are discussed in the text. (For interpretation of the references to color in this figure legend, the reader is referred to the web version of this article.)

small rivers. The I/F of Ligeia Mare in the D3 spectral window is 1.35% in the darkest areas (Fig. 6) and over Kraken Mare, I/F is 1.7% (±0.2%). That the area in Kraken Mare is brighter may be simply explained by sub-pixel rivers mixed with dry terrain. Other possibilities include light reflected by the solid surface and subsequently scattered into the beam, or the presence of solid particles at the lake surface.

3.1.3. The coastline of Ligeia Mare – comparison with radar data

The high-resolution image (cube III) allows a comparison of the VIMS observations to the radar views of Ligeia Mare that were obtained during flybys T28 and T29 in April 2007. The radar data

(Fig. 8) encompasses more than 9000 points along the shoreline. Using a Titan radius of 2575 km and the 'areaint' command of Matlab, we find that the surface area of Ligeia Mare is equal to 125,780 km². Note that a change of 500 m in the radius of Titan gives a variation of no more than 50 km².

There are two difficulties with doing the same calculations with the VIMS data. First, the choice of the contour level is critical. Second, the connection with Kraken Mare leads us to choose longitude 92°E as a western limit (Fig. 8). The values of the contour levels are equal to the number of detectors (14 detectors in the spectral window D3) times the value of I/F. Contour levels equal to 0.235 ($I/F = 1.68%$) and 0.270 ($I/F = 1.93%$) provide surface areas equal to

105,650 km^2 and 143,600 km^2, respectively. As a comparison, both values are larger than the surface area of Lake Superior (84,000 km^2), the largest of the Great Lakes.

The two contour lines 0.235 and 0.270 are very close to each other and to the radar contour along most of the shoreline, but a number of major differences are evident on the western part of Ligeia. The dark blue contour (level 0.235) does not include the northwestern part of the radar image of Ligeia Mare. This is the area that connects Ligeia Mare to region K3 of Kraken Mare (Fig. 7). In contrast, the light blue contour (level 0.270) not only includes this area but also an area in the southwest of Ligeia Mare bounded to the west by a large river (arrow 2 in Fig. 8d) originating to the northwest of lake Uvs. The seeming high density of the river network south of arrow 1 could explain the low I/F value. A comparison between the radar and VIMS mosaics does not show changes between 2007 and 2010 at the resolution of the VIMS images. Note that the radar instrument observed the southeastern part of Ligeia in December 2009 (Fig. 9) and no difference was seen when compared to the 2007 observations (Hayes et al., 2011).

Pixels close to the shoreline of Ligeia Mare (Fig. 9) have larger I/Fs, which may be due to a variety of causes including (1) the presence of sub-pixel dry areas as observed on the radar image, (2) reflection of light from high topographic features surrounding the shores, as is frequently observed at terrestrial lakes, (3) the presence of a layer of organic debris floating on the surface close to the shore, and (4) light scattered by surrounding surface into the beam of the instrument.

3.2. The small lakes

Compared to Ligeia Mare, which covers an area on the order of 125,000-km^2, the radar observations reveal small lakes, each of which has a surface area between 100- and 800-km^2 (Tables 3 and 4). The VIMS T69 observations confirm the presence of all lakes seen in the radar observations (Section 3.2.1). This strongly suggests that very dark pixels observed by VIMS in areas not covered by radar observations are also lakes. Three new lakes named by

IAU (Section 3.2.2) are called – Freeman, Cardiel and Towada. They correspond, respectively, to VIMSNN 1, 2 and 3 in Fig. 10.

3.2.1. The radar small lakes on the VIMS mosaic

Eleven of the 27 named Titan lakes (http://planetary-names.wr.usgs.gov) are located in the area mapped by the VIMS instrument during the T69 flybys (Table 3). These lakes have diameters between 14 and 50 km (0.3–1° in latitude). When data are properly map projected, for each of the radar lakes there is a corresponding dark area seen in the VIMS 5-μm images. Each area is only a few pixels wide (Fig. 10). We have determined the coordinates of the central point of these dark areas and the agreement is excellent (Table 3). The difference in the coordinates between the radar and VIMS projections has a standard deviation of 0.194° (8.7 km) and 0.264° (4.1 km) in latitude and longitude, respectively. These values are roughly the size of a VIMS pixel and smaller than the projected angular sizes of the lakes. The extremely strong correlation between the radar and VIMS observations allows us to constrain Titan's orbital parameters (Section 4.2).

Some of these lakes show larger radar contrast than others (Fig. 10). Atlitan, Cayuga, Ohrid (South part), Uvs and Vanern show strong contrast. Lanao and Logtak have lower contrast and Sevan is roughly intermediate with a dark central region and less contrast (higher albedo) at the Northern and Southern edges. The I/F in spectral window D3 ranges from 1.32% for Lanao to 1.86% for Logtak (Table 4). Lake Lanao is the darkest lake in VIMS images while being radar bright, whereas Logtak is bright at both radar and VIMS wavelengths. The penetration depth of sunlight in liquids is one to two orders of magnitude lower at 5-μm (Clark et al., 2010) than the radar penetration depth (Hayes et al., 2011), thus unless the thickness of the liquid layer is less than 1-cm, bright radar lakes should be dark in the VIMS D3 spectral data. Lake Lanao should have a liquid layer thicker than 1 cm but less than 10 cm to be dark at 5-μm and bright at radar wavelength. On the other hand, the liquid layer of lake Logtak should be less than 1 cm to be bright at both VIMS and radar wavelengths.

Finally, the dark spots on cube VI, although at lower resolution, also coincide with radar lakes (Fig. 7). For example the dark spots
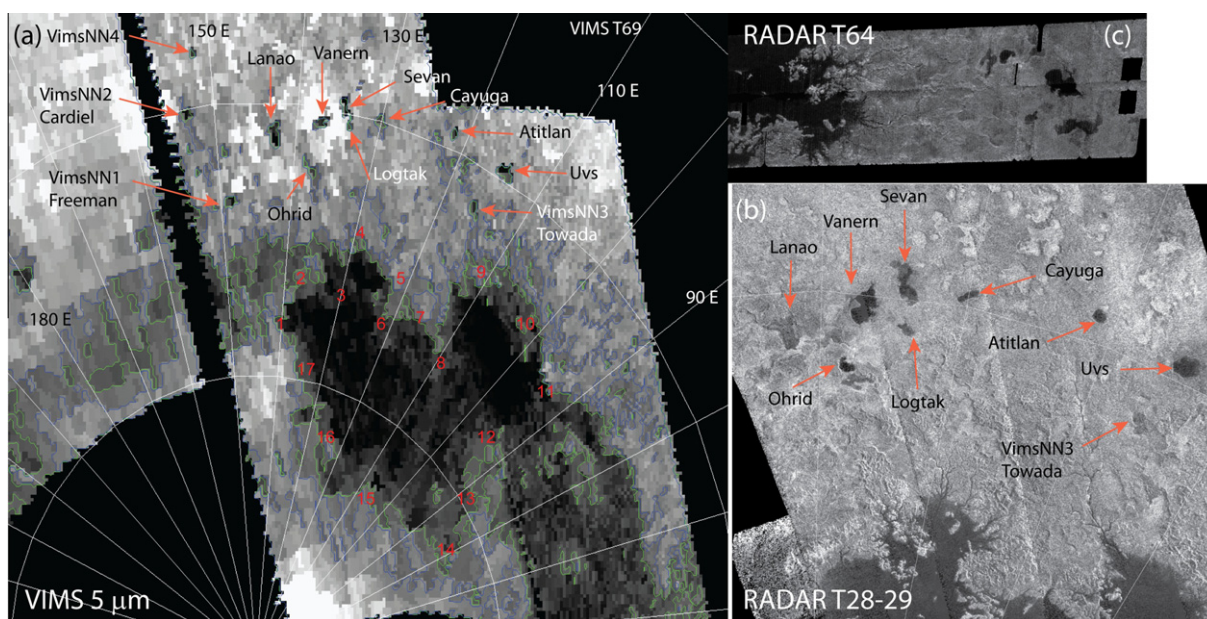

Fig. 9. The small lakes are indicated on both the VIMS mosaic taken in June 2010 (left panel) and the radar mosaic taken in April 2007 (lower right image). In addition the relevant segment of the radar path T64 (December 2009) is shown in the upper right panel. These three observations show that the small lakes have not evolved between 2007 and 2010.

Table 3
Lakes observed by VIMS cubes during the T69 flyby. Three of the new lakes have been named by the International Astronomical Union (IAU) Working Group for Planetary System Nomenclature (WGPSN) on April 7, 2011.

	Diameter	Latitude			Longitude East		
	km	USGS	Radar	VIMS	USGS	Radar	VIMS
Atitlán Lacus	13.7	69.3	69.3	69.4	121.2	121.2	121.8
Cayuga Lacus	22.7	69.8	69.7	70.0	130.0	130.0	130.3
Lanao Lacus	34.5	71.0	70.9	71.1	142.3	142.3	142.6
Logtak Lacus	14.3	70.8	70.8	70.5	133.9	133.9	133.8
Ohrid Lacus	17.3	71.8	71.9	72.3	138.1	138.1	137.8
Sevan Lacus	46.9	69.7	69.7	69.8	134.4	134.4	134.9
Uvs Lacus	26.9	69.6	69.6	69.7	114.3	114.6	114.8
Vänern Lacus	43.9	70.4	70.3	70.5	136.9	136.9	137.4
VIMSNN1 – Freeman Lacus	24	73.6		73.6	148.9		148.9
VIMSNN2 – Cardiel Lacus	22	70.2		70.2	153.5		153.5
VIMSNN3 – Towada Lacus	24	71.4	71.4	71.6	115.8	115.8	116.0
VIMSNN4				68.0			152.0

Table 4
Surface area of the small lakes. Radar observations are obtained for T28, T29 and T64 and the surface areas are sorted in this order. Logtak and Sevan have been observed at each opportunity. Four of the nine lakes were observed during the December 2009 T64 flyby. As discussed in the text, only Sevan may have shrinked significantly during the 3-year period.

|	I/F (%)	nb pixels	Pixel width (km)	Emission (°)	Incidence (°)	Surface area (km²)	High 5 μm	Radar surface (km²)
Atitlán Lacus	1.44	1.74	6.14	61.88	64.75	413	N	194/–/–
Cayuga Lacus	1.79	1.25	7.48	63.18	65.13	366	N	174/–/–
Lanao Lacus	1.32	2.83	7.47	63.50	67.92	354	N	–/695/–
Logtak Lacus	1.86	1.11	7.43	63.31	66.03	136	Y	154/164/145
Ohrid Lacus	1.74	1.21	7.39	64.87	68.45	156	y	–/199/177
Sevan Lacus	1.37	3.54	7.51	62.46	65.35	432	y	710/722/622
Uvs Lacus	1.39	7.21	6.03	63.65	65.19	591	N	509/–/–
Vänern Lacus	1.62	3.25	7.49	63.14	66.57	404	Y	–/766/778
VIMSNN1 – Freeman	1.50	1.66	7.37	65.40	70.62	217	Y	
VIMSNN2 – Cardiel	1.39	3.21	7.57	61.96	68.48	391	N	
VIMSNN3 – Towada	1.60	2.96	5.94	64.49	66.96	541	N	281/–/–
VIMSNN4	1.68	1.35	7.70	65.00	65.00	189	y	
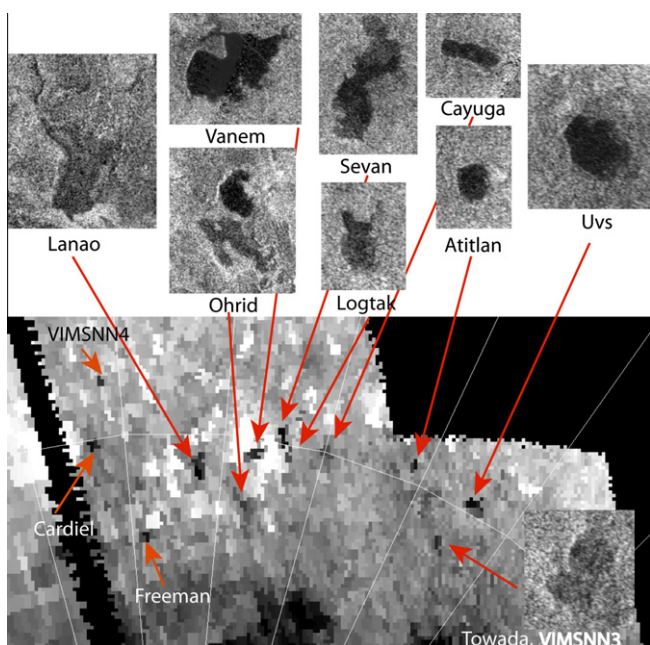
Fig. 10. Small lakes are identified on the VIMS image. When available, the radar image of each lake is also displayed. In the lower right corner is an image of the radar observation at the location of a VIMS 5-μm dark area (VIMSNN3 named Towada Lacus).

at (lat, long) = (74°N, 160°E) and (73°N, 180°E) are also seen on the radar map. That all lakes discovered by radar in 2007 are seen by

VIMS in 2010 suggests that lakes have not significantly evaporated during that period.

3.2.2. New small lakes

The VIMS mosaic displays four additional small dark areas. One of them (Towada Lacus, which is VIMSNN 3 in Fig. 10) appears relatively bright at radar wavelengths but dark at 5-μm, suggesting that it is a shallow lake, less than one meter deep (Hayes et al., 2011) through which the 2.17 cm radar wave sees the lakebed. It is also possible that this depression may have been filled with more liquid between 2007 and 2010. Indeed, Towada Lacus is potentially one of the few places seen in the T69 VIMS observations where liquid may have increased in volume since the radar observations in 2007. Nevertheless, we cannot rule out the possibility that this lake was already partially filled at the time the radar data were acquired and that the amount of liquid is just right, between 1 cm and a few tens of cms, to make it dark at 5-μm and bright at radar wavelengths.

Three other dark spots appear in the longitude range 150–160°E, an area not mapped by radar (Fig. 9). The two first spots have been named Freeman and Cardiel by the IAU panel (Tables 4 and 5).

3.2.3. The surface area of the small lakes

Determining the surface area of the small lakes constrains their evolution, a difficult measurement because the lakes cover only a few pixels at VIMS resolution and many of these pixels may partially overlay the surrounding terrains. As reported in Table 4, the mean I/F of the lakes ranges from 1.32% for Lanao Lacus to 1.86% for Logtak Lacus. The I/F of Lanao is similar to that of Ligeia. Note that Lanao is one of the largest lakes. There is a clear trend in

Table 5
New lakes observed by VIMS. The surface area of those lakes in between 400 and 500 km². Since they are a few VIMS pixels wide, the uncertainty is quite large and around 200 km².

		Latitude		Longitude East		Distance (km)		
		Radar	VIMS	Radar	VIMS	N–S	E–W	Radar
VIMSNN1	Freeman		73.6		148.9	16.0	26.0	
VIMSNN2	Cardiel		70.2		153.5	22.0	21.0	
VIMSNN3	Towada	71.4	71.6	115.8	116.0	32.0	20.0	24/20
VIMSNN4			68.0		152.0	16.5	4.2	

our data that the larger the lake, the smaller the value of I/F (Fig. 11b). Such a trend is expected for at least two reasons. First, a smaller fraction of lake pixels overlap the shoreline. Second, the I/F measurement contains less light reflected by terrains near the shore and then scattered by the atmosphere into the beam of the VIMS instrument.

We determine surface area assuming I/F linearly increases as a function of distance from I/F of a liquid (Ligeia) to that of the surrounding terrain. I/F over a liquid surface is equal to 1.32% and

Fig. 11. The surface area of the small lakes is calculated with VIMS data and is compared to the surface area determined by radar in the upper panel. The line shows equal area. As discussed in the text, there is no clear trend indicating that lakes have extended or recessed. The lower panel shows the value of I/F as a function of the surface area of the lakes to illustrate the fact that values over small lakes are larger than those over large ones because light reflected from shores is collected into the beam of the instrument. The horizontal line is the value of I/F for Ligeia Mare.

seems independent of the geometry (Fig. 6a) while the value of I/F over the surrounding terrain depends on geometry and varies linearly with $\cos(i)$ (Fig. 6b). For each lake, we use this linear trend to determine the I/F of the sub-pixel solid surface using only the darkest pixels. The values are reported in Table 4 and are compared with the surface area determined by radar observations (Fig. 11a). For Towada Lacus, we have measured the surface area of the radar depression (Fig. 10), and within the resolution of the VIMS observations, the agreement is satisfactory, suggesting that there have been no major changes between 2007 and 2010. In addition, four lakes (Ohrid, Vanern, Logtak and Sevan) were observed by the radar in December 2009 (Fig. 9), and we derive surface areas consistent in size and shape with the earlier radar measurements.

There are, however, two lakes that show differences between the VIMS and radar surface area measurements. First Lanao Lacus, the largest of the small radar lakes, seems to be larger in the radar image. Lanao's 5-μm I/F is very similar to that of the darkest spots of Ligeia, suggesting that Lanao is filled with liquid hydrocarbons. Lanao consists of three very dark pixels in the VIMS image surrounded by 12 brighter pixels whose I/F is similar to that of the surrounding terrain. Lanao Lacus is a radar-bright lake (Fig 10), suggesting that it is shallow. One explanation is that some sub-pixel, bright deposits, as seen on the shore of Ontario Lacus (Brown et al., 2008), mix with sub-pixel, dark liquid areas to provide a 'solid-surface'-like I/F. That this lake is seen to be shallow in the radar data supports this interpretation

Uvs Lacus, a radar-dark, well-defined lake, seems larger in the VIMS image than in the radar image (Fig. 11), which tempts the speculation that it grew larger between 2007 and 2010. Nevertheless, one must keep in mind that it is the only lake showing such a trend. One possible explanation is that a thin, liquid layer, transparent at radar wavelengths, covers some terrains around Uvs Lacus. Unfortunately, this lake was not observed during the radar T64 flyby in December 2009.

Finally, lakes Vanern, Sevan, and Logtak are surrounded by terrains very bright at 5-μm, evoking the possibility that these three lakes were part of a larger liquid area that is drying and leaving behind evaporate deposits (Barnes et al., 2011a). Both T29 and T64 radar images show poor correlation with the VIMS 5-μm bright terrains. The simplest interpretation for this is that the 5-μm bright material is transparent to radar because its thickness is much less that the radar wavelength.

The VIMS observations made in 2010 are a first step in the monitoring of the Northern-lake district because the lakes are now illuminated by sunlight. Future observations by both radar and VIMS should allow tighter constraints on the evolution of those lakes, as discussed in Section 4.1.

3.3. The solid surface

3.3.1. The albedo of the solid surface

This section investigates how the intensity depends on the incidence angle and provides a lower limit for the surface reflectance ($R_S(\lambda)$) or albedo at 5-μm. The surface reflectance provides information on the morphology (Soderblom et al., 2007b), the
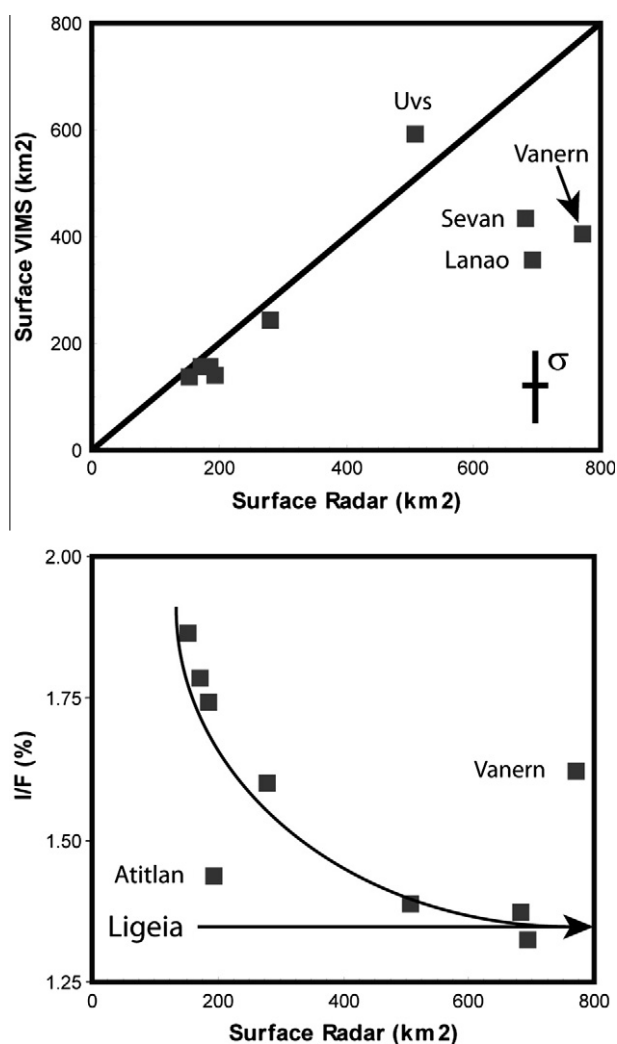
composition (McCord et al., 2006; Clark et al., 2010), and the physical state (e.g. grain size, roughness) of the surface. In the 5-μm window, there is virtually no absorption of the atmosphere. As shown by Eq. (1), I/F values linearly vary with the cosine of the incidence angle. The intercept being equal to the value over the darkest spots of Ligeia Mare (Fig. 6b) and the scattered light component from the surface of the lake being assumed to be zero in non-specular geometry, we make the assumption that this value is the single-scattering component and that the slope $S(\lambda)$ is given by:

$$S(\lambda) = R_S(\lambda) \exp(-\tau_{atm}) \qquad (2)$$

where the optical depth (τ_{atm}) is calculated using the spherical geometry (see Appendix).

Values of I/F have been plotted versus the cosine of the incidence angle for all the spectral windows. There is a clear trend for the spectral window D3 (5-μm) and the slope is equal to 3.8% per unit cosine (Fig. 6b). The dispersion around the trend is similar to the noise expected with this integration time (see Section 4.3). This slope is reasonably consistent between the three cubes IV, V, and VI with a standard deviation of 0.4%. Using the values of transmission discussed in the previous paragraph, the derived reflectance is 8% (±2%).

4. Discussion

The results described above provide new insights into (1) the evaporation rate and composition of Titan's lakes, (2) its spin rate, (3) the clarity of the 5-μm spectral window to image its surface, and (4) its hydrocarbon cycle.

4.1. Constraints on the evaporation rate and composition of the lakes

We now explore the question of the evolution of Ligeia Mare and the lakes between the radar observations in 2007 and the 2010 VIMS observations. Monitoring the evolution of the lakes is important in order to understand Titan's organic cycle. The cycle can be quickly summarized (Lunine and Atreya, 2008): methane is irreversibly photo-dissociated in the atmosphere and forms ethane; methane and ethane clouds can form and hydrocarbon precipitation may replenish the Northern lakes and are responsible for forming the rivers that have carved the equatorial highlands; more complex organic molecules form at higher altitudes; these molecules form haze particles that eventually fall to the surface and form the sands of the equatorial dunes. The amount of carbon in the three reservoirs (atmosphere, lakes, and dunes) has been estimated by Lorenz et al. (2008a). The largest uncertainty in their calculation is in the evaluation of the volume of lakes that leads to a mass of carbon between 16,000 and 160,000 GT. The upper limit is in the same range as the amount of carbon available in the atmosphere and in the dune fields. The surface area of Ligeia Mare is on the order of 125,000 km^2. If one assumes values of the lakebed slope equivalent to those found for Ontario Lacus (Hayes et al., 2010, 2011), Ligeia Mare would have a volume on the order 1600–8000 km^3 for slopes equal to 2×10^{-4} and 10^{-3}, respectively. These values provide some lower bounds awaiting values for the Northern lakes. The two other large lakes are Kraken Mare and Punga Mare. Ontario Lacus, located in the Southern hemisphere, is several times smaller. The total volume of liquid hydrocarbons present in the lakes is therefore close to the lower bound proposed by Lorenz et al. (2008a,b) on the order of 30,000 km^3. It could even be less than 10,000 km^3 if the mean depth of the lakes is less than 100 m, which is the average depth for a slope of 10^{-3}. The mass of carbon contained in the lakes would be on the order of 4000–15,000-GT depending on the amount of methane relative to

ethane. This mass is at least one order of magnitude smaller than the mass of methane contained in Titan's atmosphere that is equal to 194,000-GT if one uses the recently published profiles of temperature, pressure and methane mole fraction (Niemann et al., 2010). If one considers only the liquids present in the lakes and not the liquid hydrocarbons that may be present in the subsurface (see discussion below), the volume of Titan's liquid reservoirs is therefore small compared to its atmospheric reservoir, the opposite of the water reservoirs on Earth (Gleick, 1996). One possible explanation, as has been predicted from thermodynamic models, is that the liquid reservoirs are composed mainly of ethane whereas the very volatile methane is largely in the atmosphere.

The evaporation rate of methane can be very large because its saturation vapor pressure is quite high at Titan's surface conditions (Mitri et al., 2007). The evaporation rate also depends on the wind speed at the surface of the lake, the surface temperature, and the amount of methane in the methane/ethane mix likely to compose the lakes as is the case for Ontario Lacus (Brown et al., 2008). The brightness temperature at 75°N during the period April 2007–June 2010 is equal to 91 ± 1 K according to Jennings et al. (2009). The spectral identification of liquid ethane signatures in Ligeia Mare and the small lakes is still under investigation. The near-surface wind speed at Titan's surface is 0.3 and 1 m/s as measured by the Huygens probe in January 2005 (Tomasko et al., 2005). The environment of the Huygens Landing Site is quite different from that of the lake. The specular reflection lightcurves on Jinkpo Lacus and Kraken Mare (Barnes et al., 2011b) suggest that the wave slopes were not larger than 0.1% at the time of the observation, suggesting a low wind speed. Global circulation models (e.g. Charnay and Lebonnois, 2012) suggest wind speed of 0.3 m/s at 30 m altitude. But those models depend on the boundary conditions at the surface, including the drag velocity. Detailed modeling of the drag velocity is out of the scope of the present paper and wind velocities between 0.1 and 1 m/s are assumed as proposed in Mitri et al. (2007). For these values, Mitri et al. (2007) have determined evaporation rates of methane between 100 and 5000 kg/m^2/yr at T = 91 K, and for methane mole fraction between 100% (pure methane lake) and 35%. The largest evaporation rate is found for highest values of wind speed and methane mole fraction.

These evaporation rates have been used to calculate the production rate of methane over Ligeia Mare as well as the changes in the mare's depth, shoreline, and surface area (Fig. 12). Following the study on Ontario Lacus (Hayes et al., 2010), near-shore slopes between 2×10^{-4} and 10^{-3} (100 m per 100 km) have been investigated. The absence of changes in the location of the shoreline of Ligeia Mare between April 2007 and June 2010 (April 2007 and December 2009 for radar observations) suggests that the methane evaporation rate has been less than 50 kg/m^2/yr, which implies very slow winds and/or small amounts of methane in Ligeia Mare, and/or replenishment of methane that has balanced out the evaporation rate. These different models are worth a more complete investigation that includes use of global circulation models (GCMs) to predict the amount of rainfall that can supply methane back into the lakes. The simplest interpretation, in agreement with the present observations, is that lakes are mainly composed of ethane that has not evaporated during the winter. The rainfall of ethane by the circulation from South Pole to North Pole during the winter may explain the large amount of ethane and lack of methane that may have evaporated very early after the change of the global circulation pattern, before the Casssini spacecraft arrived at Saturn. Future observations of the evolution of the Southern Pole as the circulation is now inverting, with upwelling at Northern latitudes and downwelling at the South Pole, may help constrain the processes involved in the evolution of the lakes and the composition of the atmosphere.
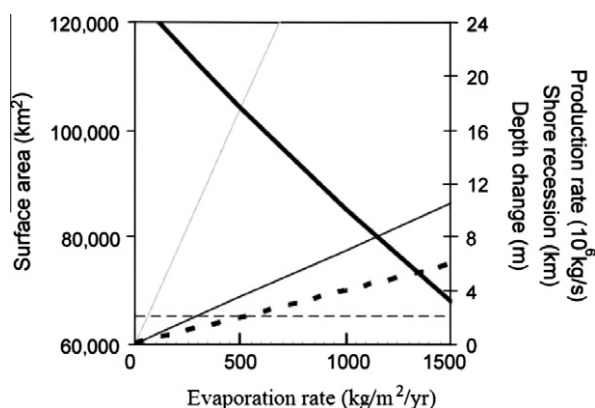
Fig. 12. The production rate of methane (bold dashed line – right vertical axis) is calculated as a function of the evaporation rate determined for a wide range of wind speeds and possible amount of methane present in Ligeia Mare (Mitri et al., 2007). The predicted changes during the period April 2007–June 2010 for Ligeia Mare are shown with the depth change in meters (plain line), shoreline recession for a slope of 2×10^{-4} (dashed line), and area (bold line – left vertical axis). The horizontal dashed line shows the resolution of 2 km. Since no recession has been observed, it suggests that the evaporation rate has been less than 50 kg/m²/yr for the parameters investigated in the present study, which suggests very slow winds and/or low relative abundance of methane in the lakes. This plot does not account for the presence of a subsurface alkanifer (see text for details).

One model that may explain the absence of noticeable evolution between 2007 and 2010 implies the presence of a subsurface reservoir of methane that would connect the lakes (e.g. Hayes et al., 2008), maintaining the amount of methane in the lakes. The depth of the methane table would increase with time as methane evaporates in the atmosphere. The large evaporation rate of methane suggests that 50 GT/yr of methane would come out of the lakes with an evaporation rate of 100-kg/m²/s and a total surface area equal to four times that of Ligeia to account for Kraken Mare, Punga Mare and all the other lakes. If there is no replenishment by rainfall, the depth change in the methane table depends on the extent of the subsurface reservoir. If one assumes that the lakes represent 2% of the total surface of the underground reservoir, the shore recession would have been only a few tens of meters with the low evaporation rate of 100-kg/m²/s. The present data cannot rule out such a model. However, one limitation of such a model is that liquid methane (and ethane) flowing into an H_2O porous crust would form very stable clathrates (Mousis and Schmitt, 2008; Choukroun and Sotin, 2012). A key piece of information would be the determination of the altitude of the lakes in order to determine whether the liquid surface defines an equipotential as it must be the case for lakes present in depressions revealing the presence of the subsurface methane table.

The evaporation rates are now compared with the photolysis destruction rate of methane in Titan's atmosphere. Methane is irreversibly destroyed by photolysis at altitudes larger than 700-km (Wilson and Atreya, 2004). Values for the loss rate of methane vary from 110 kg/s (Wilson and Atreya, 2004) to 290 kg/s in a more recent study by Lavvas et al. (2008). For a mean value of 200 kg/s, the loss of methane would be equal to 6×10^{-3}-GT/yr which is three orders of magnitude lower than the production rate of 12.5-GT/yr over Ligeia Mare for a modest evaporation rate of 100-kg/m²/s. The loss rate of methane is balanced by the formation of ethane and other heavier hydrocarbons including those that are involved in the formation of the monomers forming the haze particles. Taking the production rate of ethane from Lavvas et al. (2008) and assuming that the lakes are composed of ethane with a total mass of 4000 GT (about four times Ligeia if a bottom slope of 2×10^{-4} is assumed), then it would take 75,000 years to form the lakes from the precipitation of ethane formed by the photolysis of methane. This value is a lower limit since a lot of ethane may be stored in

the subsurface (Mousis and Schmitt, 2008; Choukroun and Sotin, 2012).

The present observation that the surface area of the lakes has not evolved between 2007 and 2010 combined with the large evaporation rates of methane predicted by recent models (Mitri et al., 2007), the large amount of hydrocarbons in the atmosphere compared to that in the lakes, the detection of ethane in Ontario Lacus (Brown et al., 2008), and the detection of ethane clouds at the Poles (Griffith et al., 2006; Lellouch, 2006) lead us to propose that the lakes are mainly composed of ethane, as suggested by the theoretical study of Cordier et al. (2009) which is based on thermodynamic equilibrium between the composition of the lakes and that of the atmosphere.

4.2. Titan's spin rate

The nine lakes identified in both the VIMS and the radar images allow us to test the hypothesis of non-synchronous rotation between April 2007 and June 2010 although the pointing errors and the sampling of the VIMS instrument make it very difficult compared to radar. Determining the value of the non-synchronous rotation is important because it provides some information on the interior structure and the possible decoupling of the icy crust from the core by a liquid ocean (e.g. Tokano et al., 2011, and references therein). Previously, observation of geological features at different times allowed the RADAR team to determine that Titan's spin axis has an obliquity of 0.3° and a spin rate of 22.57809 deg/day (Stiles et al., 2008) which is 1.11×10^{-3} deg/day faster than synchronous (22.57698 deg/day). This value was revised lower to 22.57731 ± 0.00011 deg/day (Stiles et al., 2010), still faster than synchronous by 3.3×10^{-4} deg/day.

The periodical exchange of angular momentum between the atmosphere and the crust leads to a non-synchronous rotation of the crust (Tokano and Neubauer, 2005). A more recent and complete model of angular momentum exchange (Tokano et al., 2011) predicts much smaller non-synchronous displacement with amplitudes of polar motion equal to 100 m and 1000 m for crustal thickness of 70 km and 20 km, respectively. Given that the footprint of the radar images is larger than 300 m and the resolution several times the footprint, it appears that remote-sensing observations by Cassini cannot detect the non-synchronous component related to the presence of a buried ocean, unless the thickness of the crust is less than 20 km. To date, the only observation that seems consistent with the presence of a subsurface water ocean is that of the electromagnetic signal collected by the Huygens probe, as it descended through Titan's atmosphere on January 14, 2005 (Béghin et al., 2010).

The differences between the latitudes and longitudes of the lakes observed by the radar instrument in 2007 and the VIMS instrument in 2010 have a standard deviation of 0.194° (8.7 km) and 0.264° (4.1 km) in latitude and longitude, respectively. These values are on the order of the VIMS pixel size that is equal to 5.0 km and 7.3 km for cubes IV and V, respectively (Table 1). Taking the VIMS pixel size as a limit, we find an upper bound for a potentially faster non-synchronous rotation of 2.3×10^{-4} deg/day. This value is five times smaller than the value of 1.11×10^{-3} deg/day reported by Stiles et al. (2008) and 50% smaller than the corrected valued reported by Stiles et al. (2010). In December 2009, the radar instrument acquired a path over the Eastern part of Ligeia Mare. As discussed above, no major changes were observed in the surface areas of the lakes. However, the shorelines are 'shifted' to the west. Fig. 13 illustrates this shift for Sevan Lacus that has been observed by the RADAR instrument at T28, T29 and T64. There is a clear misregistration of a few kilometers in longitude. However, the T64 location of Sevan Lacus suggests that this non-synchronous component is too large since the T28 and T29 observations that used
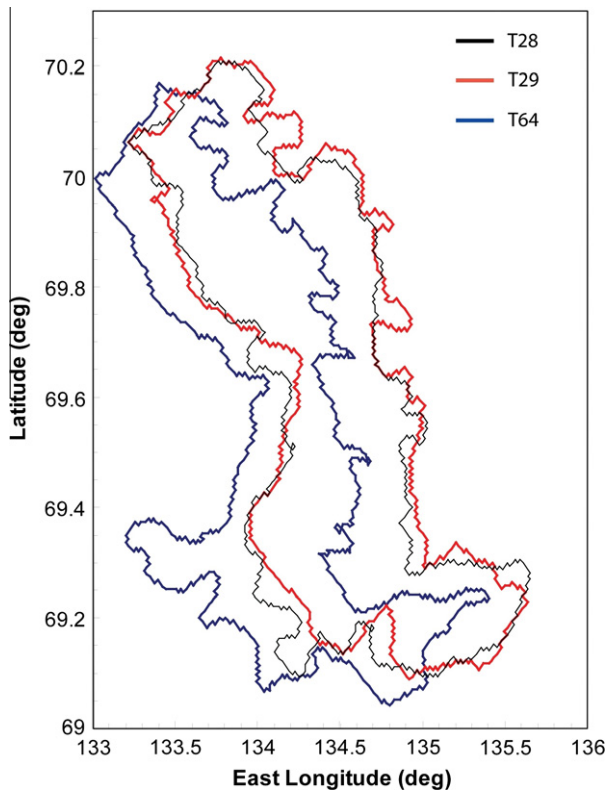
Fig. 13. Shoreline of Sevan Lacus at three different radar observations: T28, T29 and T64. The shorelines observed at T28 and at T29 differ by less than 0.1° in longitude, which is within the resolution of the radar instrument. On the other hand, the T64 shoreline is 'shifted' to the west by about 0.3- to 0.4°. The different planetary constant kernels (PCKs) used for the projection of the radar observations may explain the difference and suggest that Titan is in synchronous rotation (see Section 4.2 for details).

the later value of the non-synchronous rotation, put Sevan Lacus at larger eastern longitudes than the T64 observation that assumes synchronous rotation. Note that with a non-synchronous component of 3×10^{-4} deg/day, the location of Sevan Lacus would have been 0.7° to the east of the T28 and T29 observation. The planetary constants kernel (PCK) used to project the T28 and T29 observations is different from the kernel used for the T64 and T69 observations. We first summarize the differences in the kernels before concluding on the value of Titan's spin rate and making recommendations on the projection of Titan's remote sensing observations.

The projection of remote sensing observations on Titan's surface requires a good knowledge of the position of Titan's ellipsoid relative to the Cassini spacecraft at the time the measurements are acquired. Inversely, observations of the same geological features at different times allow the determination of Titan's orbital parameters (e.g. Stiles et al., 2008, 2010). The three parameters that are needed at a given time are the right ascension (α) and declination (δ) of Titan's spin axis and the angle (ϕ) along Titan's equator from the node to the prime meridian. The right ascension and declination of the spin axis have three components: the value at a reference time taken as J2000.0 (January 1, 2000 at 12:00 pm), the periodic variations of 691 years assuming Titan is in a Cassini state, and the temporal variations due to Saturn's precession (Seidelmann, 2007). The location of the prime meridian has two timescales that are the daily variations assuming synchronous rotation and the precession related to the Cassini state. The recommended IAU values for Titan were given by Seidelmann et al. (2007) based on the hypothesis that Titan's spin axis is perpendicular to its orbital plane and that the spin rate is synchronous:

$$\alpha = 36.41 + 2.66 \sin\left[29.8 - \frac{52.1}{365.25 \times 100} t_{IAU}\right]$$
$$- \frac{0.036}{365.25 \times 100} t_{IAU} \tag{3a}$$

$$\delta = 83.94 - 0.30 \cos\left[29.8 - \frac{52.1}{365.25 \times 100} t_{IAU}\right]$$
$$- \frac{0.004}{365.25 \times 100} t_{IAU} \tag{3b}$$

$$\phi = 189.64 + 22.5769768 \cdot t_{IAU} - 2.64$$
$$\times \sin\left[29.8 - \frac{52.1}{365.25 \times 100} t_{IAU}\right] \tag{3c}$$

where t_{IAU} is the time in days since J2000.0. The constants were used in the PCKs at the beginning of the Cassini mission (Table 6). Once the radar observations had observed several geological features at different times, it became possible to retrieve the values of the constants without making any hypothesis (Stiles et al., 2008). It was found that Titan has an obliquity of 0.3° according to the values of right ascension and declination of the spin rate axis equal to 39.4827° and 83.4273°, respectively. It was also found that Titan's spin rate was faster than synchronous (Stiles et al., 2008), but the discovery of a bug in the inversion algorithm reduced the value of the non-synchronous component by a factor of four (Stiles et al., 2010). One can note that the new solution is also characterized by a decrease in the value of the derivative of the right ascension by a factor of five. The non-synchronous rotation rate is now three times the standard deviation (Table 6) but is correlated at 98% to the temporal derivative of the right ascension (Stiles et al., 2008). These derivatives are about three times larger than the values deduced from the Cassini state equations. In other words, it is possible that the high values of the derivatives of right ascension and declination compensate for the non-synchronous value.

The present day planetary constants kernels are somewhat awkward since they use the synchronous value of the spin rate and the values of right ascension and declination of the spin axis given in Stiles et al. (2008) at a reference time equal to 19:16:25 UTC August 1, 2006:

$$\alpha = 39.4827; \quad \delta = 83.4279;$$
$$\phi = 186.5855 + 22.5769768 \cdot t_{IAU}$$

We recommend using the latest values of Stiles et al. (2010) for the values of right ascension and declination of the spin axis, the synchronous value of the spin rate, and re-incorporating the precession related to the Cassini state as well as the one related to Saturn's precession (last column in Table 6). One must note that the offset in the location of the prime meridian would be on the order of 0.4° (20 km at the equator) over the course of the Cassini mission (2004–2017) if the Cassini state is not taken into account. Although this difference sounds small, it is large enough to produce offsets in the geological maps. Future high-resolution imaging of the lakes by either the VIMS or radar teams should allow Titan's orbital parameters to be further refined. An inversion of Titan's orbital characteristics from the observations of geological features at different times should be tried with the 691 years precession imposed in the inversion code. Such a study is out of the goal of the present work but should be carried out in order to assess whether Titan is in synchronous rotation as are all other satellites of Saturn.

Table 6
Constants used in the Planetary Constants Kernels (PCKs) at different times of the mission. The IAU values were used at the beginning of the mission. The values in the first column are the IAU values at time 19:16:25 UTC August 1, 2006. The values from Stiles et al. (2008) were used for the radar observations T28 and T29. Starting in 2009, the PCKs use right ascension and declination from Stiles et al. (2008). The last column gives values of PCKs that we recommend.

	IAU	Stiles et al. (2008)	Stiles et al. (2010)	PCK-2009	Rec. PCK
Pole RA (PRA) (°)	37.589	39.483 (25)	39.493 (25)	39.4827	39.493
Pole Dec (PD) (°)	83.6710	83.4279 (24)	83.4368 (24)	83.4279	83.4368
Spin rate (SR) (deg/day)	22.5770	22.57809 (11)	22.57731 (11)	22.5769768	22.5769768
dPRA/dt (deg/century)	−2.2031	−30.1 (4.2)	−6.5 (4.2)	0	−2.2031
dPD/dt (deg/century)	−0.1252	−0.05 (0.36)	−0.22 (0.36)	0	−0.1252
dSR/dt (deg/day/century)	0	0.0523 (50)	0.0247 (50)	0	0

4.3. Observing Titan's surface at 5 μm

Observing Titan's surface at optical wavelengths is challenging because most of the photons are absorbed by different gases present in the atmosphere except in some spectral windows. But even in these spectral windows, the problem is challenging because atmospheric hazes scatter the light. The present oblique observations of the lakes with large values of incidence and emission angles definitely demonstrate the potential of the 5-μm spectral window to image Titan's surface.

Observations of solar occultations by the VIMS instrument (Bellucci et al., 2009) provide a value of the transmission at 5-μm for altitudes larger than 80 km. These observations suggest that the density of aerosols follows an exponential law with a scale height of 59 km. Measurements made by the Huygens probe during its descent in Titan's atmosphere suggest that the density becomes constant at about 80 km down to the surface. With this information, it is possible to derive the one-way transmission as a function of the incidence or emission angle (Fig. 14). In order to estimate the total transmission, one needs to multiply the incoming transmission by the outgoing transmission. The vertical transmission is found to be 90%, meaning that nadir observations with vertical illumination would give a nearly transparent total transmission of 81%.

When the incidence angle or emission angle increases, one can see that the transmission does not decrease significantly. The transmission is still 80% for an incidence angle of 70°. Nadir observations with this kind of incidence angle would provide 72% transmission. The present observations also demonstrate that transmission is still quite good at incidence angle close to 85°.

For comparison, the transmission at the closest spectral window (2.72-μm) is poor since one cannot see the difference between the lakes and the solid surface (Fig. 4). Tomasko et al. (2008) and Bellucci et al. (2009) find that the optical depth varies as λ^{-2}. These papers discuss the significance of dependence as well as the variations of this wavelength dependency with altitude. With such a value, the optical depth of the 2.72-μm light is multiplied by a factor
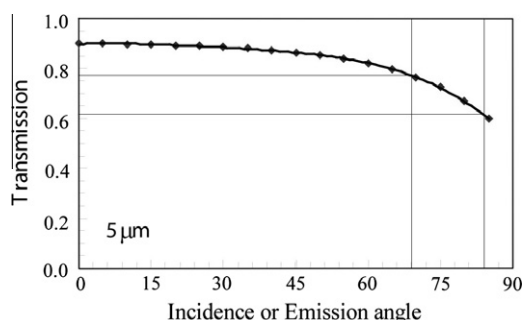
of 3.3. For the geometry of the present observations, the transmission is divided by a factor of 6 at 2.72-μm compared to the transmission at 5-μm.

The signal/noise (S/N) ratio is much smaller at 5-μm than at 2-μm (Fig. 3b). Observations of the Sun before and after occultation by Titan's atmosphere provide a way to monitor the value of S/N. For an integration time of 40 ms, it is equal to 600 and 20 at 2-μm and 5-μm, respectively. This S/N ratio nearly increases as $\sqrt{t}$ and $\sqrt{N}$ where t and N are the integration time and the number of detectors, respectively. When using the 5 μm window (14 detectors between 4.9 and 5.1 μm), the S/N increases by a factor 3.3 instead of 3.7 = $\sqrt{14}$. Cube VI was acquired with an integration time of 240-ms. Therefore, the value of S/N is ~170 for solar observations, which suggest a noise on the order of 0.6% of the solar flux. The value of I/F is on the order of 1–3% (Fig. 6), which is a factor 2–5 larger than the noise. Over the lake (Fig. 6a), the variability is on the order of the noise, as is the variability about the trend line on the solid surface. Although the observations provide a surface reflectance on the order of 8% (Section 3.3), the noise level is such that small variations in the surface reflectance cannot be detected.

The 5-μm window has proven to be very good at seeing Titan's surface although the S/N ratio is low. With the VIMS instrument, increased values of S/N can be obtained by increasing the integration time. This is done at the expense of coverage. During the extended mission, more observations at large integration times (1 s) will be acquired. They are coupled with observations at small integration time to avoid saturation at 2-μm. Future missions to Titan should take advantage of the transparency of the 5-μm window in order to map Titan's surface.

4.4. Implication for the origin of Titan's methane and its carbon cycle

The lakes are one of Titan's hydrocarbon reservoirs (Fig. 15). As described in Section 4.1, there are several lines of evidence that point towards ethane being the major constituent. On the other hand, the amount of ethane in the atmosphere is quite small, on the order of 2 GT with the concentrations given by Lavvas et al. (2008) and the new (P, T) profiles from Niemann et al. (2010). The precipitation of ethane at the Poles formed the lakes. Moreover, liquid ethane is likely to interact with the crust. If the crust is made of water ice, then the reaction with ethane would turn it into ethane clathrates (Mousis and Schmitt, 2008). If the crust is made of methane clathrates as proposed by Tobie et al. (2006), then liquid ethane would substitute to methane to form ethane clathrates (Choukroun and Sotin, 2012). Moreover, the expulsed methane would be released in the atmosphere and would partly replenish it (Fig. 15). This process has been explored to explain Titan's shape (Choukroun and Sotin, 2012). It would have operated over several hundreds of Myr in order to explain the observed difference between the equatorial radius and the polar radius at the present estimated precipitation rate of ethane.

A large fraction of the methane destruction ends with the formation of aerosols that fall on the surface and form the dunes
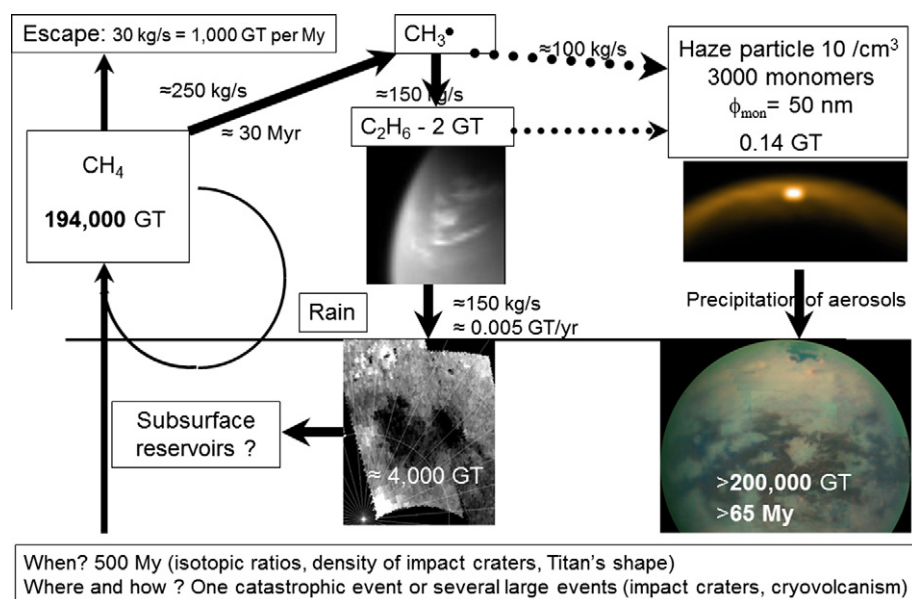

Fig. 14. Transmission through Titan's atmosphere at 5-μm as a function of the incidence or emission angle showing that this window is well suited for surface observations through Titan's haze although the solar flux is weak at this wavelength.

Fig. 15. Summary of the carbon reservoirs that are discussed in the present study. The main reservoirs are the atmospheric methane and the surface dunes. Additional reservoirs may be present in the subsurface and in the deep interior. The transformation from the original methane to the dune final product implies the formation of ethane and subsequent formation of aerosols. The amount of ethane in the atmosphere is small compared to the amount estimated in the lakes (see text for more details).

(Fig. 15). The amount of methane necessary to form the dunes cannot be precisely determined since the volume of the dunes is not well constrained and the chemical composition of the sand is not known. On the other hand, the mass of aerosols in Titan's atmosphere can be estimated using values proposed by both Tomasko et al. (2008) and Bellucci et al. (2009) for the number of monomers (3000) in the aerosols. Using a density of 800 kg/m^3, and ignoring variations of haze opacity with latitude (Rannou et al., 2010), we find that the total mass of aerosols is 0.07 GT. Rannou et al. (2010) suggest that the haze opacity increases by a factor of 3 from the South Pole to the equator, and then decreases by a factor of 2 between 30-N and the North Pole. These variations may result in different values for the reference density of aerosols. If the density is scaled by a factor of 2 to account for higher opacity at the equator, then the mass becomes a fraction of GT, but still orders of magnitudes less than the amount of organic particles that compose the dunes as estimated by LeGall et al. (2011) at more than 200,000 GT of carbon. A mass of methane between 150,000- and 400,000-GT may have been necessary to form the dunes. A photolysis loss rate between 100- and 200-kg/s would provide the necessary material in a timescale between 25- and 150-Myr if only this process was implied.

Aerosols are formed in the neutral atmosphere in a narrow layer about 40-km thick located at about 400-km altitude (Rannou et al., 2004) and in the ionosphere (Wahlund et al., 2009). Coupled dynamics-microphysics models of Titan's atmosphere developed by Rannou et al. (2003, 2004) use formation rates between 10- and 100-kg/s. In these models, aerosols form only in the neutral atmosphere. Aerosols formed at higher altitudes at a rate of 3- to 30-kg/s (Wahlund et al., 2009) fall and mix with the ones formed at 400 km altitude. These different numbers suggest that the formation rate of aerosols must be comprised between 10 and 130 kg/s. With a value of 0.14 GT of aerosols in the atmosphere (Fig. 15), the residence time is equal to 35 and 450 years. The production rate can also be used to assess the time required to form the dunes covering Titan's surface. With a value of 200,000 GT, this time is between 50- and 630-Myr.

These numbers are consistent with the age of atmospheric methane proposed by Mandt et al. (2012). They are also consistent with the age of Titan's surface. The density of impact craters on Titan's surface is much smaller than that on other Saturnian satellites such as Rhea, Dione and Tethys (Wood et al., 2010). The density is not uniform (Wood et al., 2010) with the Xanadu region having a much larger density and the Belet dune field with a much smaller one. Converting the density of impact craters into absolute ages is difficult because the cratering history of the Saturn system is poorly known. Two independent models (Artemieva and Lunine, 2005; Korycansky and Zahnle, 2005) give ages of a given crater distribution that can differ by a factor 5 (Lorenz et al., 2007). Wood et al. (2010) conclude that the density of impact craters is generally consistent with the evolutionary model of Tobie et al. (2006) which predicts that only during the last half billion years has Titan had a thick enough crust to be stable from volcanic overturn and to preserve impact features. A more recent study (Neish and Lorenz, 2012) gives a crater retention age between 200 Myr and 1 Gyr.

All these observations suggest that a major event occurred on Titan some hundreds of Myr ago. During this event, methane would have been released in the atmosphere and a new crust formed. Alternatively, after the new crust was formed, methane could have been released during several cryovolcanic events. But evidences for cryovolcanic features on Titan are sparse. The methane released in the atmosphere would form ethane and aerosols that would end up in the polar crusts and equatorial dune fields, respectively (Fig. 15).

5. Conclusions

This work has shown that the VIMS instrument can observe the polar regions where the illumination conditions are difficult and there is little affect due to atmospheric scattering in the transmission at 5-μm. Furthermore, these observations show that the surface area of Ligeia Mare has not significantly changed, at least by more than a few kilometers, between the radar observations in 2007 and the VIMS observations in 2010, suggesting that little evaporation has taken place. This result is difficult to reconcile with evaporation models unless methane is a very minor constituent of the lakes. These data provide meaningful estimates of the size of the different carbon reservoirs on Titan. A simple model of methane outburst, a few hundreds of Myr ago, followed by

ethane rain in the polar regions and aerosols falling on the surface would explain the observations. The observations have allowed us to retrieve a value of 8% for the reflectance of the solid surface at 5-μm. The present VIMS observations and the recent T64 radar observations question the existence of measurable non-synchronous component of the spin-axis rate. Future work should address this issue in order to provide adequate planetary constant kernels (PCKs) for the projection of the different remote sensing information acquired by the Cassini/Huygens mission. The next opportunity for VIMS to observe the Northern lakes has been implemented and will occur in July 2012 during the T85 flyby. It will provide the first chance to see changes of the Northern lakes between two VIMS observations.

Acknowledgments

Appendix A

This section describes the calculation of the optical depth (τ_{atm}). It can be expressed as a function of the scattering cross section (σ_{scat}) and the density of the scatterers (n) that depends on the altitude (z):

$$\tau_{atm} = \int_{D_{inc}}^{0} \sigma_{Scat}(\lambda)n(z)dl + \int_{0}^{D_{emi}} \sigma_{Scat}(\lambda)n(z)dl \qquad (A.1)$$

where dl is differential path length. In expression (A.1), D_{inc} and D_{emi} are the maximum value of the optical path length in the scattering atmosphere for incidence and emission angles, respectively. Since the values of incidence and emission angles are large, the plane-parallel approximation cannot be used and the D_{inc} and D_{emi} are therefore:

$$D_{inc} = R\cos(i)\left[\sqrt{1 + \frac{H(H+2R)}{R^2\cos^2(i)}} - 1\right] \quad \text{and}$$

$$D_{emi} = R\cos(e)\left[\sqrt{1 + \frac{H(H+2R)}{R^2\cos^2(e)}} - 1\right] \qquad (A.2)$$

where the thickness (H) of the atmospheric scattering layer is smaller than 300-km at 5-μm according to solar occultation data (Bellucci et al., 2009). Note that if $H/R\cos(i)$ and $H/R\cos(e)$ are small, then Eq. (A.2) can be approximated by the more usual form: $D_{inc} + D_{emi} = H(1/\cos(i) + 1/\cos(e))$. One important aspect of estimating the optical depth is that the density of scatterers increases as altitude decreases down to 80 km with a scale height of ~65 km (Tomasko et al., 2008; Bellucci et al., 2009), becoming constant in the last 80 km (Tomasko et al., 2008). The altitude (z) is determined at each distance (l) from a point on the surface as:

$$z_{inc} = R\left[\sqrt{1 + \frac{l(l+2R\cos(i))}{R^2}} - 1\right] \quad \text{and}$$

$$z_{emi} = R\left[\sqrt{1 + \frac{l(l+2R\cos(e))}{R^2}} - 1\right] \qquad (A.3)$$

As discussed in Section 4.3, the optical depth at 5-μm is so small that even with the large emission and incidence angles, the transmission is between 60% and 80% for incidence or emission angles

equal to 85° and 70°, respectively. This transmission may be even larger at the Poles if the density of aerosols is smaller there as suggested by numerical simulations (Rannou et al., 2010).

References

Aharonson, O., Hayes, A., Lunine, J.I., Lorenz, R.D., Elachi, C.,2009.Anasymmetric distribution of lakes on Titan as a possible consequence of orbital forcing. Nature Geoscience 2, 851–854.

Artemieva, N., Lunine, J.I., 2005. Impact cratering on Titan. II – Global melt, escaping ejecta, and aqueous alteration of surface organics. Icarus 175, 522–533.

Atreya, S.K. et al., 2006. Titan's methane cycle. Planet. Space Sci. 54, 1177–1187.

Barnes, J.W., Brown, R.H., Soderblom, L., Buratti, B.J., Sotin, C., Rodriguez, S., Le Mouèlic, S., Baines, K.H., Clark, R., Nicholson, P.D., 2007. Global-scale surface spectral variations on Titan seen from Cassini/VIMS. Icarus 186, 242–258.

Barnes, Jason.W., Bow, J., Schwartz, J., Brown, R.H., Soderblom, J.M., Hayes, A.G., Vixie, G., Le Mouelic, S., Rodriguez, S., Sotin, C., Jaumann, R., Stephan, K., Soderblom, L.A., Clark, R.N., Buratti, B.J., Baines, K.H., Nicholson, P.D., 2011a. Organic sedimentary deposits in Titan's dry lakebeds: Probable evaporite. Icarus 216, 136–140.

Barnes, J.W. et al., 2011b. Wave constraints for Titan's Jingpo lacus and Kraken Mare from VIMS specular reflection lightcurves. Icarus 211, 722–731.

Béghin, C., Hamelin, M., Sotin, C., 2010. Titan's native ocean revealed beneath some 45 km of ice by a Schumann-like resonance. C.R. Geosci. 342, 425–433.

Bellucci, A., Sicardy, B., Drossart, P., Rannou, P., Nicholson, P.D., Hedman, M., Baines, K.H., Burrati, B., 2009. Titan solar occultation observed by Cassini/VIMS: Gas absorption and constraints on aerosol composition. Icarus 201, 198–216.

Brown, R.H. et al., 2004. The Cassini Visual and Infrared Mapping Spectrometer investigation. Space Sci. Rev. 115, 111–168.

Brown, R.H. et al., 2008. The identification of liquid ethane in Titan's Ontario Lacus. Nature 454, 607–610.

Charnay, S., Lebonnois, S., 2012. Two boundary layers in Titan's lower troposphere inferred from a climate model. Nat. Geosci. 5, 106–109. http://dx.doi.org/10.1038/NGEO1374.

Choukroun, M., Sotin, C., 2012. Is Titan's shape caused by its meteorology and carbon cycle? Geophys. Res. Lett. 39, L04201.

Clark, R.N. et al., 2010. Detection and mapping of hydrocarbon deposits on Titan. J. Geophys. Res. 115, E10005.

Combes, M. et al., 1991. Martian atmosphere studies from the ISM experiment. Planet. Space Sci. 39, 189–197.

Cordier, D., Mousis, O., Lunine, J.I., Lavvas, P., Vuitton, V., 2009. An estimate of the chemical composition of Titan's lakes. Astrophys. J. 707, L128. http://dx.doi.org/10.1088/0004-637X/707/2/L128.

Drummond, S.A., Burr, D.M., Cartwright, R., Black, B.A., Perron, J.T., 2011. Global mapping and morphologic classification of Titan fluvial features. Lunar Planet. Sci. 42, Abstract #1919.

Elachi, C. et al., 2004. RADAR: The Cassini Titan radar mapper. Space Sci. Rev. 115, 71–110.

Gleick, P.H., 1996. In: Schneider, S.H. (Ed.), Water Resources, Encyclopedia of Climate and Weather, vol. 2. Oxford University Press, New York.

Griffith, C.A. et al., 2006. Evidence for a Polar Ethane Cloud on Titan. Science 313, 1620–1622.

Hayes, A.G. et al., 2008. Hydrocarbon lakes on Titan: Distribution and interaction with a porous regolith. Geophys. Res. Lett. 35, L09204. http://dx.doi.org/10.1029/2008GL033409.

Hayes, A.G. et al., 2010. Bathymetry and absorptivity of Titan's Ontario Lacus. J. Geophys. Res. 115, E09009.

Hayes, A.G., Aharonson, O., Lunine, J.I., Kirk, R.L., Zebker, H.A., Wye, L.C., Lorenz, R.D., Turtle, E.P., Paillou, P., Mitri, G., Wall, S.D., Stofan, E.R., Mitchell, K.L., Elachi, C., the Cassini RADAR Team, 2011. Transient surface liquid in Titan's polar regions from Cassini. Icarus 211, 655–671.

Jennings, D.E. et al., 2009. Titan's surface brightness temperatures. Astrophys. J. 691, L103–105.

Korycansky, D.G., Zahnle, K.J., 2005. Modeling crater populations on Venus and Titan. Planet. Space Sci. 52, 695–710.

Lavvas, P.P., Coustenis, A., Vardavas, I.M., 2008. Coupling photochemistry with haze formation in Titan's atmosphere – Part II: Results and validation with Cassini/Huygens data. Planet. Space Sci. 56, 67–99.

Le Mouelic, S. et al., 2012. Dissipation of Titan's North polar cloud at Northern spring equinox. Planet. Space Sci. 60, 86–92.

LeGall, A., Janssen, M.A., Wye, L.C., Hayes, A.G., Radebaugh, J., Savage, C., Zebker, H., Lorenz, R.D., Lunine, J.I., Kirk, R.L., Lopes, R.M.C., Wall, S., Callahan, P., Stofan, E.R., Farr, T., the Cassini Radar Team, 2011. Cassini SAR, radiometry, scatterometry and altimetry observations of Titan's dune fields. Icarus 213, 608–624.

Lellouch, E., 2006. Titan's zoo of clouds. Science 311, 186–187.

Lorenz, R.D. et al., 2007. Titan's young surface: Initial impact crater survey by Cassini RADAR and model comparison. Geophys. Res. Lett. 34, L07204. http://dx.doi.org/10.1029/2006GL028971.

Lorenz, R.D. et al., 2008a. Titan's inventory of organic surface materials. Geophys. Res. Lett. 35, L02206.

Lorenz, R.D. et al., 2008b. Titan's rotation reveals an internal ocean and changing zonal winds. Science 319, 1649–1651.

Lunine, J.I., Atreya, S., 2008. The methane cycle on Titan. Nat. Geosci. 1, 159–164.

Mandt, K.E. et al., 2012. The 12C/13C ratio on Titan from Cassini INMS measurements and implications for the evolution of methane. Astrophys. J. 749 (160), 14. http://dx.doi.org/10.1088/0004-637X/749/2/160.

McCord, T.B. et al., 2006. Composition of Titan's surface from Cassini VIMS. Planet. Space Sci. 54, 1524–1539. http://dx.doi.org/10.1016/j.pss.2006.06.007.

Mitri, G., Showman, A.P., Lunine, J.I., Lorenz, R.D., 2007. Hydrocarbon lakes on Titan. Icarus 186, 385–394.

Mousis, O., Schmitt, B., 2008. Sequestration of ethane in the cryovolcanic subsurface of Titan. Astrophys. J. 677, L67–L70.

Neish, C.D., Lorenz, R.D., 2012. Titan's global crater population: A new assessment. Planet. Space Sci. 60, 26–33.

Niemann, H.B. et al., 2005. The abundances of constituents of Titan's atmosphere from the GCMS instrument on the Huygens probe. Nature 438, 779–784.

Niemann, H.B. et al., 2010. Composition of Titan's lower atmosphere and simple surface volatiles as measured by the Cassini–Huygens probe gas chromatograph mass spectrometer experiment. J. Geophys. Res. 115, E12006. http://dx.doi.org/10.1029/2010JE003659.

Rannou, P., McKay, C.P., Cabane, R.D., 2003. A model of Titan's haze of fractal aerosols constrained by multiple observations. Planet. Space Sci. 51, 963–976.

Rannou, P., Hourdin, F., McKay, C.P., Luz, D., 2004. A couple dynamics-microphysics model of Titan's atmosphere. Icarus 170, 443–462.

Rannou, P., Cours, T., Le Mouelic, S., Rodriguez, S., Sotin, C., Drossart, P., Brown, R.H., 2010. Titan haze distribution and optical properties retrieved from recent observations. Icarus 208, 850–867.

Rodriguez, S., Paillou, P., Dobrijevic, M., Ruffié, G., Coll, P., Bernard, J.M., Encrenaz, P., 2003. Impact of aerosols present in Titan's atmosphere on the Cassini radar experiment. Icarus 164, 213–227.

Rodriguez, S. et al., 2006. Cassini/VIMS hyperspectral observations of the Huygens Landing Site on Titan. Planet. Space Sci. 54, 1510–1523.

Seidelmann, P.K. et al., 2007. Report of the IAU/IAGWorking Group on cartographic coordinates and rotational elements: 2006. Celestial Mech. Dyn. Astr. 98, 155–180.

Sobolev, V.V., 1975. Light Scattering in Planetary Atmospheres. Pergamon, New York.

Soderblom, L.A. et al., 2007a. Topography and geomorphology of the Huygens Landing Site on Titan. Planet. Space Sci. 55 (13), 2015–2024.

Soderblom, L.A. et al., 2007b. Correlations between Cassini VIMS spectra and RADAR SAR images: Implications for Titan's surface composition and the character of the Huygens probe landing site. Planet. Space Sci. 55 (13), 2025–2036. http://dx.doi.org/10.1016/j.pss.2007.04.014.

Soderblom, J.M., Soderblom, L.A., Barnes, J.W., Brown, R.H., Griffith, C.A., Stephan, K., Jaumann, R., Sotin, C., Baines, K.H., Buratti, B.J., Clark, R.N., Nicholson, P.D., 2012. Modeling specular reflections from hydrocarbon lakes on Titan. Icarus, http://dx.doi.org/10.1016/j.icarus.2012.05.030.

Sotin, C. et al., 2005. Release of volatiles from a possible cryovolcano from near-infrared imaging of Titan. Nature 435 (7043), 786–789.

Stephan, K., Jaumann, R., Brown, R.H., Soderblom, J.M., Soderblom, L.A., Barnes, J.W., Sotin, C., Griffith, C.A., Kirk, R.L., Baines, K.H., Buratti, B.J., Clark, R.N., Lytle, D.M., Nelson, R.M., Nicholson, P.D., 2010. Specular reflection on Titan: Liquids in Kraken Mare. Geophys. Res. Lett. 37, L07104.

Stiles, B.W. et al., 2008. Determining Titan's spin state from Cassini radar images. Astron. J. 135, 1669–1680.

Stiles, B.W. et al., 2010. Erratum: "Determining Titan's spin state from Cassini radar images" (2008, Astron. J. 135, 1669); Astron. J. 139, 311.

Stofan, E.R. et al., 2007. The lakes of Titan. Nature 445, 61–64.

Thekaekara, M.P., 1973. Solar energy outside the Earth's atmosphere. Sol. Energy 14, 109–127.

Tobie, G., Lunine, J., Sotin, C., 2006. Episodic outgassing as the source of atmospheric methane on Titan. Nature 440, 61–64.

Tokano, T., Neubauer, F., 2005. Wind-induced seasonal angular momentum exchange at Titan's surface and its influence on Titan's length-of-day. Geophys. Res. Lett. 32, L24203. http://dx.doi.org/10.1029/2005GL024456, 2005.

Tokano, T., Van Hoolst, T., Karatekin, Ö., 2011. Polar motion of Titan forced by the atmosphere. J. Geophys. Res. 116, E05002. http://dx.doi.org/10.1029/2010JE003758, 2011.

Tomasko, M.G. et al., 2005. Rain, winds and haze during the Huygens probe's descent to Titan's surface. Nature 438, 765–778.

Tomasko, M.G. et al., 2008. A model of Titan's aerosols based on measurements made inside the atmosphere. Planet. Space Sci. 56, 669–707.

Turtle, E.P. et al., 2009. Cassini imaging of Titan's high latitude lakes, clouds, and south-polar surface changes. Geophys. Res. Lett. 36, L02204.

Wahlund, J.E. et al., 2009. On the amount of heavy molecular ions in Titan's ionosphere. Planet. Space Sci. 57, 1857–1865.

Wilson, E.H., Atreya, S.K., 2004. Current state of modeling the photochemistry of Titan's mutually dependent atmosphere and ionosphere. J. Geophys. Res. 109, E06002.

Wood, C.A., Lorenz, R., Kirk, R., Lopes, R., Mitchell, K., Stofan, E., The Cassini RADAR Team, 2010. Impact craters on Titan. Icarus 206, 334–344.